FACULTY OF INFORMATION TECHNOLOGY AND ELECTRICAL ENGINEERING

Jukka Kaipala

AUTOMATIC SEGMENTATION OF BONE TISSUE FROM COMPUTED TOMOGRAPHY USING A VOLUMETRIC LOCAL BINARY PATTERNS BASED METHOD

Master's Thesis
Degree Programme in Computer Science and Engineering
February 2018

Kaipala J. (2018) Automatic segmentation of bone tissue from computed tomography using a volumetric local binary patterns based method. University of Oulu, Degree Programme in Computer Science and Engineering. Master's Thesis, 66 p.

ABSTRACT

Segmentation of scanned tissue volumes of three-dimensional (3D) computed tomography (CT) images often involves—at least partially—some manual process, as there is no standardized automatic method. There is a need to develop fully automatic approaches, not only to improve the objectivity of the task, but also to increase the overall speed of the segmentation process. Here we extend a 3D local binary patterns (LBP) -based trabecular bone segmentation method with adaptive local thresholding and additional segmentation parameters to make it more robust yet still perform adequately when compared to traditional user-assisted segmentation. We estimate parameters for the new automated adaptive multiscale LBP-based 3D segmentation method (AMLM) in our experimental setting, and have two micro-CT (μCT) scanned bovine trabecular bone tissue volumes segmented by both the AMLM and two experienced users. Comparison of the results shows superior performance of the AMLM suggesting the strong potential for this solution to perform automatic bone segmentation.

Keywords: LBP, micro-CT, trabecular bone, segmentation.

Kaipala J. (2018) Luukudoksen automaattinen segmentointi tietokonetomografiakuvista kolmiulotteisella local binary patterns -perustaisella menetelmällä. Oulun yliopisto, tietotekniikan tutkinto-ohjelma. Diplomityö, 66 s.

TIIVISTELMÄ

Skannattujen kudosrakenteiden segmentointi kolmiulotteisista (3D) tomografiakuvista tehdään usein ainakin osittain manuaalisesti, sillä standardoitua automaattista menetelmää ei ole. Täysin automatisoitujen lähestymistapojen kehitys on tarpeen, sillä se parantaisi sekä segmentoinnin objektiivisuutta että sen kokonaisnopeutta. Tässä työssä laajennamme automatisoitua local binary patterns (LBP) -perustaista trabekulaarisen luun 3D-segmentointimenetelmää adaptiivisella paikallisella kynnystyksellä ja segmentoinnin lisäparametreilla tavoitteenamme vahvistaa menetelmää mutta säilyttää silti riittävä suorituskyky verrattuna perinteiseen käyttäjäavusteiseen segmentointiin. Arvioimme koejärjestelyssämme parametrit uudelle automatisoidulle adaptiiviselle moniasteikkoiselle LBP-pohjaiselle 3D-segmentointimenetelmälle (AMLM), ja teetämme sekä AMLM:n avulla että kahden kokeneen käyttäjän toimesta binäärisegmentoinnit kahdelle mikro-tietokonetomografialla (μTT) tuotetulle kuvalle naudan trabekulaarisesta luukudoksesta. Tulosten vertailu osoittaa AMLM:n suorituskyvyltään selkeästi paremmaksi, mikä antaa vahvan viitteen tämän menetelmän soveltuvuudesta automatisoituun luusegmentointiin.

Avainsanat: LBP, mikro-TT, trabekulaarinen luu, segmentointi.

TABLE OF CONTENTS

FOREWORD

The article was designed with and supervised by Jérôme Thevenot, Miguel Bordallo López and Simo Saarakkala, of the University of Oulu. No animals were knowingly harmed in the making of this thesis.

Helsinki, 14.12.2017

Jukka Kaipala

ABBREVIATIONS

2D	two-dimensional
3D	three-dimensional
AMLM	automated adaptive multiscale LBP-based 3D segmentation method
BV/TV	bone volume fraction
CBCT	cone-beam computed tomography
CC	cyclomatic complexity
CT	computed tomography
GT	ground truth
LBP	local binary patterns
MBIR	model-based iterative reconstruction
OA	osteoarthritis
OP	osteoporosis
PVE	partial volume effect
SSIM	structural similarity
SD	standard deviation
Tb.Th	trabecular bone thickness
VOI	volume of interest

$\boldsymbol{B}$	threshold image
C	constant adjustment parameter for mean filtered image
$\boldsymbol{f}$	original image
$\boldsymbol{f}_{\mu}$	mean filtered image
N_1	inner interpolation sphere vertex-count parameter
N_2	outer interpolation sphere vertex-count parameter
R_1	inner interpolation sphere radius parameter
R_2	outer interpolation sphere radius parameter
T	percent adjustment parameter for mean filtered image
W	mean thresholding image kernel size parameter

μ_{δ}	mean percent error
μCT	micro-computed tomography

1. INTRODUCTION

This thesis presents a novel automated multiscale local binary patterns (LBP) based three-dimensional (3D) segmentation method (AMLM), which extends an existing trabecular bone tissue specific segmentation method with customized adaptive local thresholding to improve its robustness. We estimate scanner and resolution specific thresholding parameters using bone phantom scans at three resolutions, and then evaluate the adaptive thresholding by comparing automated and traditional binarization results of two bovine subchondral bone samples scanned with the same equipment.

The ultimate purpose the work was to improve the diagnostics of joint and bone diseases. Our approach was based on automatic segmentation of trabecular bone from computed tomography (CT). The context is the configuration and development of an existing automated multiscale LBP-based segmentation method (MLM) that was implemented in MATLAB. The method was designed specifically for trabecular bone tissue, and its main purpose is to accurately determine the shape of continuous border regions between dense bone and other tissue for detailed structural analysis.

The results of this thesis have been collected and rewritten into a conference article that was accepted and presented at the Scandinavian Conference of Image Analysis, SCIA, and can be found under the following reference:

> Kaipala J, Bordallo López M, Saarakkala S & Thevenot J (2017) Automatic segmentation of bone tissue from computed tomography using a volumetric local binary patterns based method. Scandinavian Conference in Image Analysis (SCIA), Tromsø, Norway. [1]

1.1. Objectives

The thesis focuses on the development of automated trabecular bone segmentation, and specifically the MATLAB scripted MLM implementation, which is the problem domain of the research.

Our original objective was to improve the performance of the scripted MLM and define data specific segmentation parameters:

1) Optimization of MATLAB segmentation scripts for speed and robustness
2) Definition of segmentation parameters based on the data to analyze

Additionally, we were going to support the work with:

3) Assessment of the effects of image resolution and artifacts
4) Comparison of the segmented data between different imaging modalities such as micro-CT (μCT) and cone-beam CT (CBCT)

These objectives evolved, as writing a conference paper from this study has been suggested. To improve the relevance of the manuscript to be submitted, the main focus was given to the suggested methodology as a novel approach for segmentation. The following new main objectives were set after we were already familiar with the

technical details of the segmentation method and could hypothesize ways to build on its functionality.

5) Extension of an LBP-based segmentation method with volumetric adaptive thresholding and additional label
6) Comparison of parameterized automatic thresholding results with traditional user-assisted thresholding

1.2. Contributions

The scientific contributions of this thesis have both methodological and practical applications.

The first set of contributions is referred to the analysis and optimization of the existing scripts for the computation of the segmentation. In this context, we describe how the segmentation scripts were optimized for speed and robustness, and apply quantitative methods to both the original and optimized versions of the scripts to estimate our success. We measure the relative performance of script versions by segmenting the same test data with compatible configurations.

The methodological contributions include the extension of the original segmentation method with customized adaptive local thresholding and an additional label to improve its robustness. To our knowledge, the method has not been adapted to volumetric segmentation of medical data before, and our work is also the first attempt to combine the underlying adaptive thresholding methods this way.

For this, we extend the method with an additional segmentation label. Our addition of the new label is based on the hypothesis that it gives the AMLM conceptual symmetricity compared to the original border label, and its inclusion would complement the set of likely partial volume voxels in the tissue border area. It also gives more calculation options to improve the accuracy of subsequent volumetric LBP analysis. We will not be able to evaluate its effect, because the actual structural analysis is outside the scope of this work, but we can estimate its effect on the performance and make sure it remains acceptable.

We introduce two empirical methods for dynamic configuration of scanner and resolution specific segmentation parameters. We estimate binarization parameters by extracting trabecular bone structural parameters from µCT scanned phantom segmented using different configurations at three levels of resolution, and evaluate results by comparing them to the corresponding nominal values. To adjust LBP-based neighborhood parameters, we evaluate segmentations created with different parameters by their structural similarity (SSIM) to the ground truth (GT).

We evaluate the configured adaptive binarization method by comparing its performance and GT similarity to corresponding values measured for traditional user-assisted binarization using the same trabecular bone volumes.

Additionally, we assess the effects of image resolution and artifacts in our experiments, and compare segmentations of µCT and CBCT scans of a trabecular bone sample.

1.3. Structure

As stated before, this master thesis extends our published conference paper. The structure of the thesis follows common conventions of scientific research.

The rest of this thesis is organized as follows:

Chapters 2, 3, 4 and 5 present the theoretical background. First, we justify the research by introducing common bone and joint diseases, and by explaining how they are linked with the microstructure of trabecular bone. We give overview of digital image segmentation and its challenges, and introduce MLM as a method specifically tailored for the segmentation of trabecular bone structure. We provide background on the general principles of CT imaging and typical visual artifacts that are encountered with this modality.

Chapter 6, related to the materials used, gives more detailed account of the equipment and methods used in this work.

Chapter 7 presents the results, describing the details of our work process, and presenting measurements and other observations from our research.

Chapter 8 discusses and interprets the results and the significance of individual findings in the context of our objectives. Chapter 9 draws conclusions of the overall work and its significance.

Appendices support our summarized results with details of the measurements to define the segmentation parameters.

2. ANALYSIS OF OSTEOARTHRITIC TRABECULAR BONE

Osteoarthritis (OA) is a major degenerative joint disease. [2] It affects articular bone, cartilage and synovium, especially in weight-bearing joints like the hip and the knee. Its end-stage symptoms include disabling pain and stiffness, as subchondral bone deforms, and adjacent cartilage tissue calcifies or wears out. The disease develops gradually, and while it may take decades before any life-affecting symptoms, their appearance is often synonym to an advanced stage of the condition.

Early diagnosis of OA improves its treatment results. Mature cartilage tissue is resilient but has very limited self-repair ability. Moreover, clinical treatment is generally palliative and does not heal damaged joint tissues. Primary treatments include pain relief and supportive measures that slow OA progress, with joint replacement surgery as last option. Detection of OA signs at an early stage is beneficial, because it gives more treatment options and can result in improved long-term health. [3,4]

Analysis of trabecular bone structure can support diagnosis and research. There are many phenotypes of OA, as well as internal and external factors and mechanisms that affect its onset. [5] Articular health is a system of fine balance between chemical and mechanical factors, and OA develops as a symptom of this imbalance, whether initiated by mechanical trauma or other factors. Therefore, early and reliable diagnosis of OA can benefit from several different methods. Analysis of subchondral bone microstructure is one possible approach.

Metabolically active trabecular bone is constantly under natural process of resorption and remodeling, and this bone formation process responds to mechanical and biological factors. [5,6] Trabecular bone microstructure is known to reflect the health of the articular bone and cartilage. Late OA remodeling includes such changes as increased bone mineral density and more plate-like structure. There is also some indication that trabecular bone defects can precede cartilage damage, although not by a causal relationship. [7]

Volumetric trabecular bone structure is difficult to image and analyze in a clinical setting. [8] The size of trabecular features is typically a few hundred micrometers or less, and microscale resolution must be attained *in vivo* with low radiation dose, which induces noise and resolution related artifacts. Nevertheless, the data can be linked with textural parameters derived from other modalities. it is also possible to image trabecular bone structure *ex vivo*, which can help identify potential disease indicators.

OA is our primary focus in this context, but the potential of trabecular bone microstructure analysis is not limited just to OA. The bone resorption mechanism causes also age-related bone loss i.e. osteoporosis (OP). Therefore, it is likely that similar trabecular bone analysis methods could be used to assess the stages of both diseases.

LBP has been recently adapted for segmentation and analysis of trabecular bone. [9,10] μCT and volumetric LBP-based analysis was used successfully on subchondral trabecular bone samples in a previous research. There, most structural and textural parameters correlated strongly with severity of OA. The same characterization applies also to bone tissue changes in OP. [11]

LBP-based trabecular bone segmentation is under-investigated subject, and there is room for research and experimentation. LBP-based segmentation (and analysis) has already been automated with MATLAB scripts, but it is still a work in progress.

3. SEGMENTATION PROBLEM

Image segmentation is a process that classifies image constituents into two or more groups that represent some distinct aspects of the data to highlight relevant image features for further analysis. The simplest segmentation task is binarization by thresholding, which defines imaged object boundaries by dividing constituents into background and foreground depending on whether their grayscale value meets a selected gray-value threshold. There are several more complex thresholding methods that are classifiable by the locality of their thresholds, by the assumptions made about voxel connectivity, and by the extent that they can be automated. Examples of common methods are Otsu's method [12], region growing methods [13], and shape-based methods like geodesic active contours [14].

Segmentation is one of the most difficult problems in image processing and remains an active area of development. [15]. Despite decades of research, there exists no universal segmentation method that would produce best results in all cases. One reason is that there is no absolute GT, and therefore, a single right answer. Another reason is that segmentation methods vary in their sensitivity to artifacts and image quality. Most segmentation methods are specialized and perform best on the object and modality they were designed for. In practice, segmentation methods are considered and selected separately for each task. 3D segmentation faces additional challenges due to large datasets, and because computationally intensive segmentation algorithms, like shape-based algorithms, require much more memory and calculation power than simple thresholding.

Nowadays, volumetric imaging is often used in the medical field, from devices such as magnetic resonance imaging or CT, and several applications require volumetric segmentation of tissues. [16] One of the biological structures that is relevant to assess in 3D is the metabolically active trabecular bone, this one being at upmost interest in studies of musculoskeletal disorders. Pathological bone conditions such as OA and OP are linked to small changes in trabecular bone microstructure that can be assessed from 3D μCT images. [17]

However, while high-resolution imaging can be used for *in vitro* CT studies, the clinical resolution is limited due to radiation levels which must be kept low. [18] Low-resolution imaging increases the impact of artifacts such as the partial volume effect (PVE), and leads to challenging segmentations. PVE comprises a class of imaging resolution related artifacts that limit how well a reconstructed voxel can represent its object location. [19]

Segmentation should be ideally a completely automatic process, but this remains a difficult goal to reach. The lack of generic automated algorithms increases the effect of human factors like time consumed, interpersonal variance and systematic error. Together these factors have negative effect on 3D scanned image segmentation and subsequent structural analysis as well as clinical diagnosis.

LBP-based methods represent a promising but still under-investigated alternative solution to conventional manual and semi-automatic 3D segmentation methods. [9,16]

4. MULTISCALE LBP-BASED 3D SEGMENTATION

This chapter describes the baseline method utilized for the segmentation of the bone. This is a multistage process that utilizes CT scans as an input and produces a segmented and labelled image.

4.1. Overview

The bone analysis process consists of three parts: 1) Estimation of segmentation parameters, 2) automatic volumetric LBP-based segmentation, which is further divided to binary thresholding and edge labeling, and 3) volumetric LBP-based analysis of the segmented bone microstructure from segmentation results from the previous step. This last step is outside of the scope of this work, however. These steps are illustrated in Figure 1.

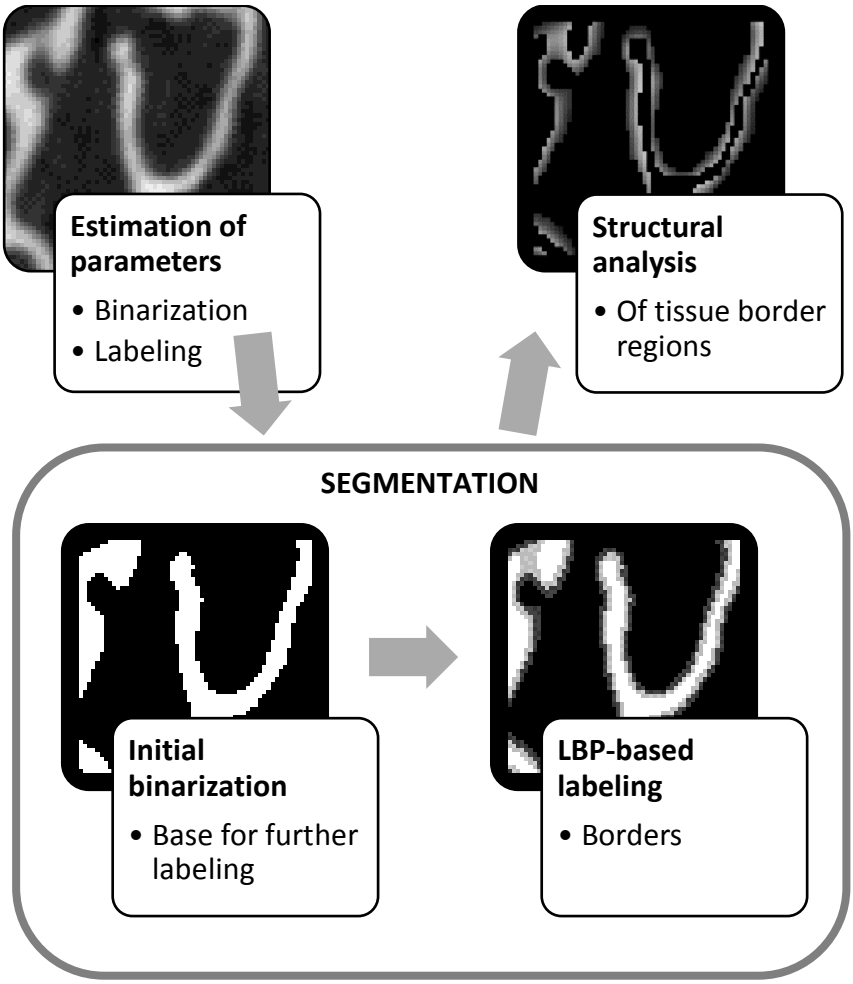

Figure 1. Overview of the trabecular bone analysis process.

The segmentation method is not fully automatic in the sense that it requires configuration of several parameters, whose optimal values depend on the scanning setting (that is, medium, modality, resolution, etc.). These parameters affect the

automatic segmentation, which is critical for the accuracy of the subsequent structural analysis of the segmentation.

The first proper segmentation step, binarization, defines tissue region and provides threshold values that are used in the labeling step.

The final segmentation step, LBP-based labeling, takes the original volume and its binarization mask from the previous step and labels regions that represent tissue borders labels. The resulting reduced data set—trabecular bone border regions—is base for the structural analysis step, which investigates markers linking the bone microstructure and articular or bone diseases. The continuous geometry and gray-values of the labeled border voxels are all-important for the analysis. However, these border regions are also naturally sensitive to PVE, especially at low resolutions, where large voxels are less likely to coincide with the tissue border.

The segmentation method is still a work in progress, and it has parameters whose values are arbitrary. One such parameter is the scaling factor of the global thresholding level. Global binarization can cause problems anyway, for example when artifacts cause variation in local intensity over the segmented area, which distorts the segmentation result.

We replaced the original binarization step with a locally adaptive method, hypothesizing that it would improve the binarization result in a general case without degrading the overall segmentation speed too much. Secondly, we increased the information content of the segmentation result with an additional fourth label. We took a methodical brute force approach to parameter configuration. That is, we segmented with several sets of parameters and selected those that compared best against ideal results, separately for both binarization and labeling steps.

4.2. Introduction to LBP

Here we discuss briefly the principle of LBP before explaining how its principle has been applied to the segmentation method and how it is configured.

LBP is an image operator that assigns each pixel a descriptor value, which is obtained by thresholding gray-values of a pixel neighborhood point pattern and interpreting the result as a binary number. This LBP code can be used to classify different neighborhood patterns.

LBP code can be regarded as a binary number, where bit positions correspond to ordered set of neighborhood points. A bit value represents the logical relation of a neighborhood point to the center pixel gray-value. Figure 2 illustrates the principle of the 8-bit LBP code calculation using a circular neighborhood with eight ordered members.

The circular LBP operator takes or interpolates the P neighboring point gray-values g_p at radius R from the center pixel, thresholds them using the center pixel gray-value g_c, then encodes non-negative results at (zero-based) neighbor positions p into binary values 2^p and calculates their sum. [20]

The original LBP method was introduced for image texture analysis, where it has been shown to be both computationally efficient and insensitive to global variations of grayscale values. [20–23] The LBP operator is traditionally used to classify texture patterns, which has little to do with actual segmentation.

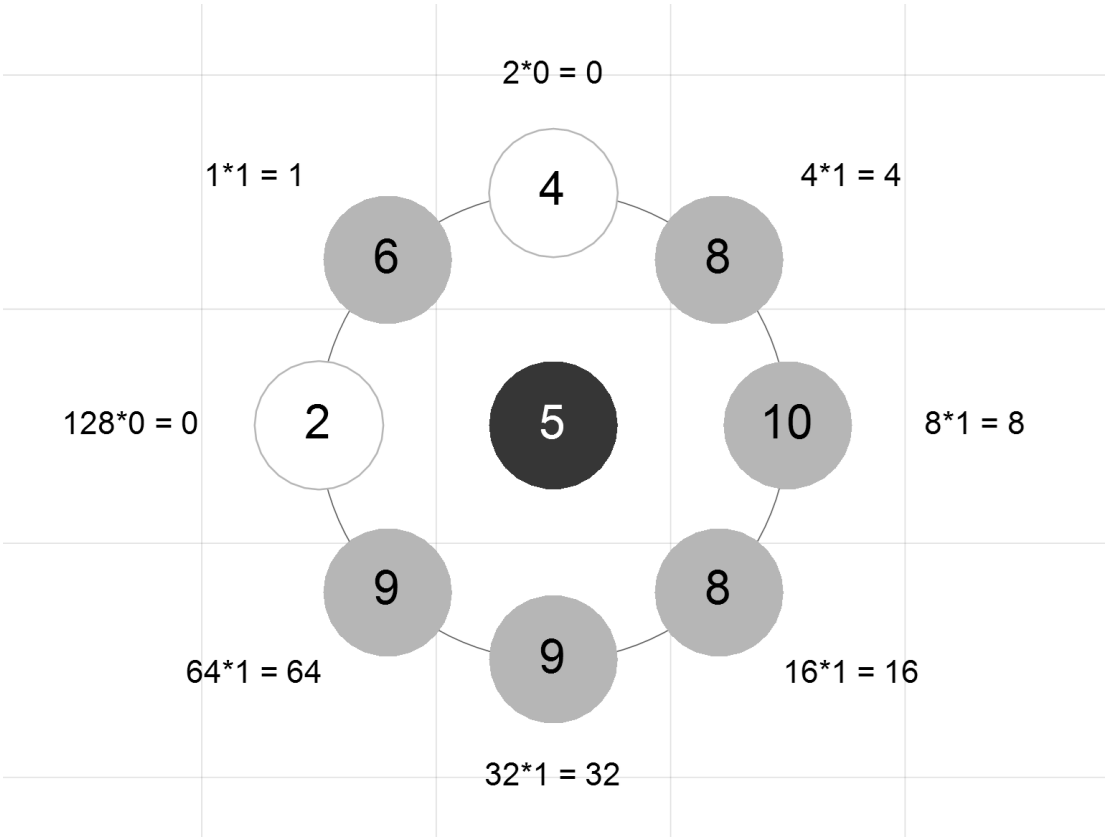

Figure 2. 8-bit LBP code calculation of a pixel (solid black) in plane with eight LBP neighbors (gray). The code value is the sum of the bit values of the neighborhood elements (solid gray) whose interpolated gray-value (number inside the element) equals or exceeds the center pixel gray-value. In this example, the LBP code is 1+4+8+16+32+64 = 125.

The original LBP neighborhood consisted of the eight pixels adjacent to a center pixel, but the model has since been extended to larger and circularly shaped neighborhoods with bilinear interpolation. [20] The above figure represents an early variant with the original rectangular grid replaced by a circular neighborhood. The circle does, however, correspond more naturally to the volumetric neighborhood of the LBP-based segmentation, which will be discussed next.

4.3. Multiscale LBP-based 3D segmentation

MLM is a novel automated segmentation method that has been suggested as an alternative to the common binary thresholding for analyzing bone microstructures in CT images. [16] It has recently been validated for the segmentation of μCT scans of osteoarthritic trabecular bone and the subsequent statistical analysis. [9]

MLM is based on LBP but differs from it in certain ways. Major difference from traditional LBP is that patterns are evaluated using a global threshold instead of the voxel gray-value or other local threshold. In other words, pattern elements are defined in effect by their tissue membership instead of their relative local activity.

In addition, MLM examines neighborhood patterns on two nested levels in a 3D volume, firstly for the voxel itself and secondly for its inner neighborhood points. Figure 3 illustrates the geometry of the MLM neighborhood. The method groups and

analyzes the nested patterns to label continuous bone structures and their edges and to set disconnected bone voxels to the background.

This figure represents the LBP-inspired volumetric neighborhood of the segmentation method. Its structure corresponds to the local neighborhood pattern in the previous LBP image but in three dimensions. In general, the inner neighborhood consists of a spherical set of N_1 vertices at radius R_1, and the full outer neighborhood set comprises N_1 patches of small spherical caps further away at radius R_2 in the direction of each inner neighborhood point. Outer neighborhood patches are based on the polar vertex neighborhood of a vertex sphere with radius R_2 and N_2 uniformly distributed vertices.

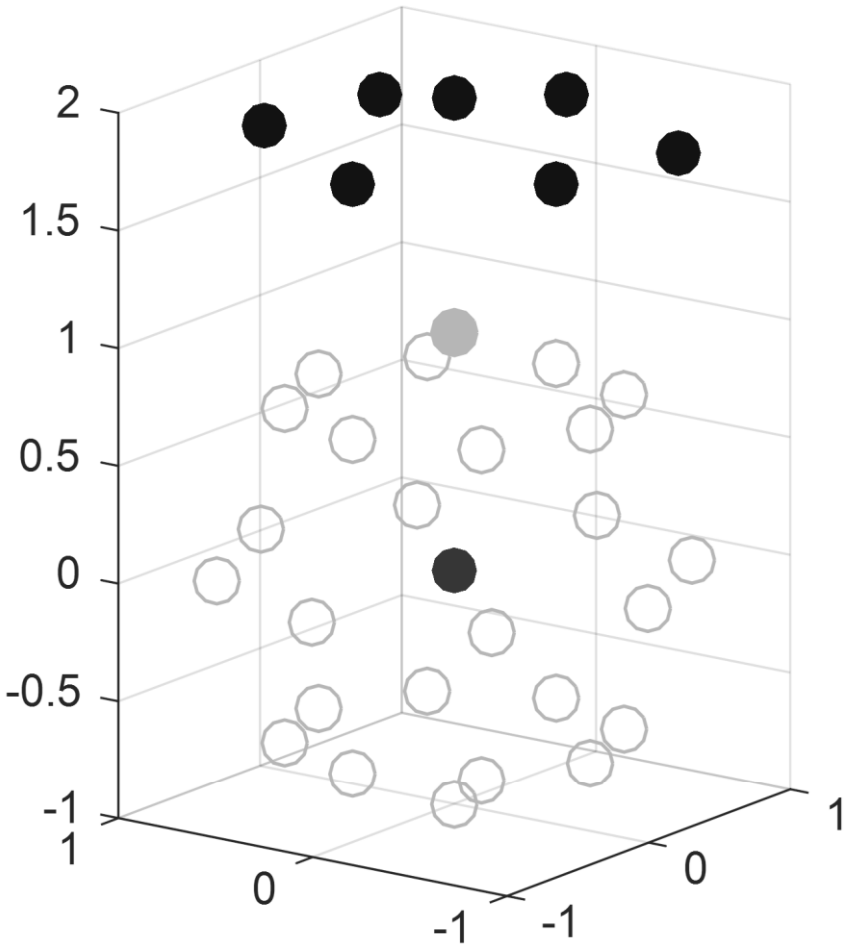

Figure 3. Partial multiscale neighborhood of a voxel (solid black, at the origo of this frame) in the default neighborhood configuration. The spherical inner neighborhood at radius $R_1 = 1$, consists of 26 points (gray). The remaining points (solid black) at radius $R_2 = 2$ at the top represent the outer neighborhood cluster of the topmost inner neighborhood point (solid gray).

Functionally, the method models oriented continuous local surfaces in 3D to define edges of complex trabecular tissue and to and assign edge labels to corresponding voxels.

Firstly, in contrast to regular LBP operators, the multiscale LBP-based method does not actually describe patterns. The difference is subtle, but the segmentation

variant evaluates a minimal set of patterns to assign a (border) label to the center voxel as needed.

Secondly, pattern constituents are evaluated based on the relation of their gray-values to a separately calculated threshold value instead of the center voxel like in LBP. The center voxel is also compared to the threshold value, which therefore becomes an implicit super-layer in this neighborhood hierarchy.

Thirdly, the segmentation method extends the basic pattern with additional nested 7-point[1] neighborhood (or sometimes two) for each spherical neighborhood point. Every point in the spherical inner neighborhood projects similar umbrella-dome-shaped nested neighborhood away from the center voxel. This nested neighborhood level represents the sense of depth and direction, which improves tissue edge detection and classification of its borders.

The theoretical number of possible patterns is so large that it makes the estimated number of particles in the observable universe seem vanishingly small in comparison. However, the segmentation method is required to label only border voxels, in addition to making possible adjustments to the initial binarization. Therefore, the method combines patterns, treats neighborhoods as units, and evaluates them only when necessary.

4.4. Local mean based thresholding

Binarization by thresholding is a basic type of segmentation in medical imaging. The calculation of the gray-value threshold is the main problem, and there are two main approaches. The threshold value can be global, i.e. the same gray-value for all voxels, or it can be calculated for each voxel. Global thresholding methods are generally fast and automate efficiently. Local thresholding methods are less sensitive to artifacts like noise and local differences in attenuation. They are also computationally more complex than global methods, and they do not scale as well to large volumes.

Since artifacts are common in medical images, global thresholding does not always produce satisfactory segmentation. There are modalities like CBCT imaging where local (adaptive) thresholding is considered more reliable.

There are two promising two-dimensional (2D) local methods described in the literature: Bradley's (mean) method and adaptive (mean) thresholding. Both methods have existing MATLAB implementations that are so fast and scalable in 2D that they could be expected to perform reasonably well also when adapted to 3D.

An important feature of both mean thresholding methods is that the calculation of neighborhood mean values can be conducted very efficiently by using a pre-calculated integral image, which eliminates explicit sum calculation for local means. The revised calculations comprise simple addition and subtraction of indexed values, and the number of operations is fixed regardless of the kernel size W. This makes mean filtering based adaptive thresholding methods fast compared to e.g. median filtering. The performance gain is advantageous in 3D image analysis, where datasets can be very large. Hence, for this application, these computationally simple and relatively fast mean adaptive thresholding algorithms present therefore a promising local alternative to global thresholding.

[1] Certain neighborhood parameters may produce 6-point neighborhoods.

Bradley's Method

Bradley's method was introduced for 2D binarization of digital grayscale documents with varying levels of illumination [24]. The principle of the method is simple. First, a local threshold array $\boldsymbol{B}(x, y)$ is created by mean filtering (blurring) a 2D source image $\boldsymbol{f}(x, y)$ and downscaling the result $\boldsymbol{f}_{\mu}(x, y)$ by T percent. The source image is then compared to the threshold map, and each pixel with gray-value equal to or greater than its corresponding local threshold value is assigned to the foreground.

The method requires two external parameters, (isotropic) mean filter kernel size W and downscaling adjustment percentage T. The actual threshold map $\boldsymbol{B}(x, y)$ is

$$\boldsymbol{B}(x, y) = \left(1 - \frac{T}{100}\right) \boldsymbol{f}_{\mu}(x, y) \ , \tag{1}$$

where the mean filtered image $\boldsymbol{f}_{\mu}$ can be expressed as

$$\boldsymbol{f}_{\mu}(x, y) = \frac{1}{W^2} \sum_{i=x-r}^{x+r} \sum_{j=y-r}^{y+r} \boldsymbol{f}(x, y) \ . \tag{2}$$

Here, r is the axial extent of the filter mask from its center, and W is short for $2r + 1$, being the actual width of the mean filter kernel.

Adaptive thresholding

The other 2D method, adaptive mean thresholding [25], is very much like Bradley's method. The difference is that it subtracts an arbitrary constant value C from the mean filtered image instead of downscaling it with a weight factor. The threshold calculation can be done using the following:

$$\boldsymbol{B}(x, y) = \boldsymbol{f}_{\mu}(x, y) - C \ . \tag{3}$$

This adaptive thresholding method is known also as mean–C in some other contexts.

Hybrid thresholding

Our thresholding method is a generalized 3D adaptation of two existing 2D binary thresholding methods, the adaptive mean thresholding and Bradley's method. The volumetric extension of the mean formula can be expressed as

$$\boldsymbol{f}_{\mu}(x, y, z) = \frac{1}{W^3} \sum_{i=x-r}^{x+r} \sum_{j=y-r}^{y+r} \sum_{k=z-r}^{z+r} \boldsymbol{f}\,(x, y, z) \ , \tag{4}$$

and the corresponding hybrid formula that incorporates both previously introduced 2D methods becomes

$$\boldsymbol{B}(x, y, z) = \left(1 - \frac{T}{100}\right) \boldsymbol{f}_{\mu}(x, y, z) + C \ . \tag{5}$$

The hybrid method requires three external parameters: mean filter kernel size W, local mean volume scaling percent adjustment T and constant adjustment C.

To our knowledge, this is the first time in published research that these 2D methods have been extended to 3D.

4.5. AMLM as an extension of MLM

AMLM is an extension of MLM with the same basic principles. The extended method can be described mostly in the same way as MLM. The most significant difference between MLM and AMLM is that the latter integrates the previously introduced hybrid adaptive method to threshold and evaluate neighborhood patterns. This and other distinguishing features of AMLM are highlighted in Figure 4.

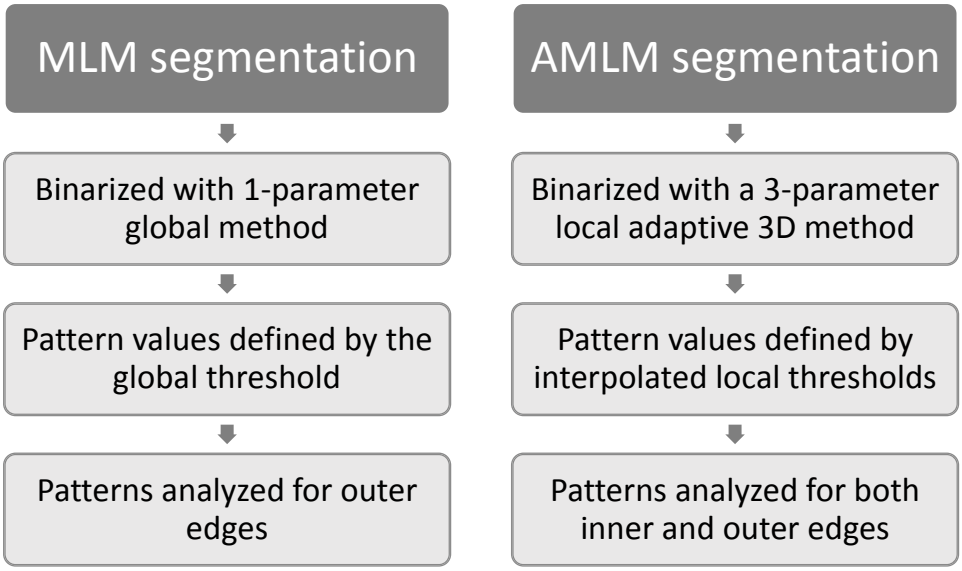

Figure 4. Major features that make the workflow of AMLM segmentation different from the segmentation with MLM.

MLM uses a global value for its initial thresholding and LBP calculations. We replaced it with a map of local threshold values for this experiment to make the method more robust, especially if the gray-value intensity varies over the imaged region. This does not come without a tradeoff, as the additional complexity results in a slight negative effect on the performance, but still neglectable for the present experiment.

A related but distinct new feature of AMLM is that pattern constituents (and tissue membership in general) are defined by the relations to interpolated local thresholds instead of a single global threshold. We hypothesize that improves the robustness of the pattern evaluation in the LBP-based segmentation step, although the dynamic interpolation step also makes the method less efficient.

The original MLM segmentation explored and labeled only the voxels lying immediately outside the binarized tissue and labeled them as border. We reversed the classifying algorithm to label also the inner border region. The additional analysis step naturally adds to the segmentation time.

5. ARTIFACTS IN COMPUTED TOMOGRAPHY

5.1. Overview

Artifact is any feature of a reconstructed image of a scanned object that differs from the ideal image. [26] In practice, reconstruction algorithms cannot perfectly model physical media and measurement devices, which means that artifacts are inevitable.

Any phase of CT image acquisition can and will cause artifacts. First, artifacts are inherent to the physical imaging process. Secondly, reconstruction models approximate the image acquisition process because of practical reasons or lack of data. Thirdly, scanned media or scanning equipment may possess features or imperfections that further break the model. In any case, artifacts are side effects of the image acquisition process and do not represent features of the imaged object.

Artifacts lower the quality a scanned image, and it is important to minimize their effect. Post-processing can remove many artifacts from a reconstructed CT volume.

5.2. Principles of computed tomography

The idea behind CT is based on mathematical reconstruction of a volume from measurements of multiple x-ray projections at different angles through a succession of planes. [27] Figure 5 illustrates the principle of the projection data acquisition process.

The first CT scanners were built in the early 1970s. In a simple early model, linear projections were obtained by translating a single narrow x-ray beam and detector in parallel steps across the imaging plane, creating a view for each orientation. The measurement plane was then positioned to the next slice, and the acquisition process was repeated. Although later scanner generations have significantly improved on the basic design with fanned beams and multiple detectors, among other things, the basic principles remain the same.

Actual CT images are calculated or estimated from the view projections with a suitable reconstruction process on a powerful computer. Several different reconstruction methods have been introduced, including algebraic reconstruction technique and filtered back projection. Advanced computer technology has enabled more developed methods like model-based iterative reconstruction (MBIR). Best algorithms produce higher quality images with thinner slices and lower doses, which is desirable for clinical imaging.

Voxels of initial projection images are not necessarily isotropic. Slice step and thickness values vary, and helical CT acquires projections in a single slice that advances smoothly along its rotation axis, instead of step by step. Adjacent layers (whether helical or planar) may be interleaved or even have a gap between them. Regardless of the design, reconstruction algorithms conventionally produce a stack of slices with isotropic voxels.

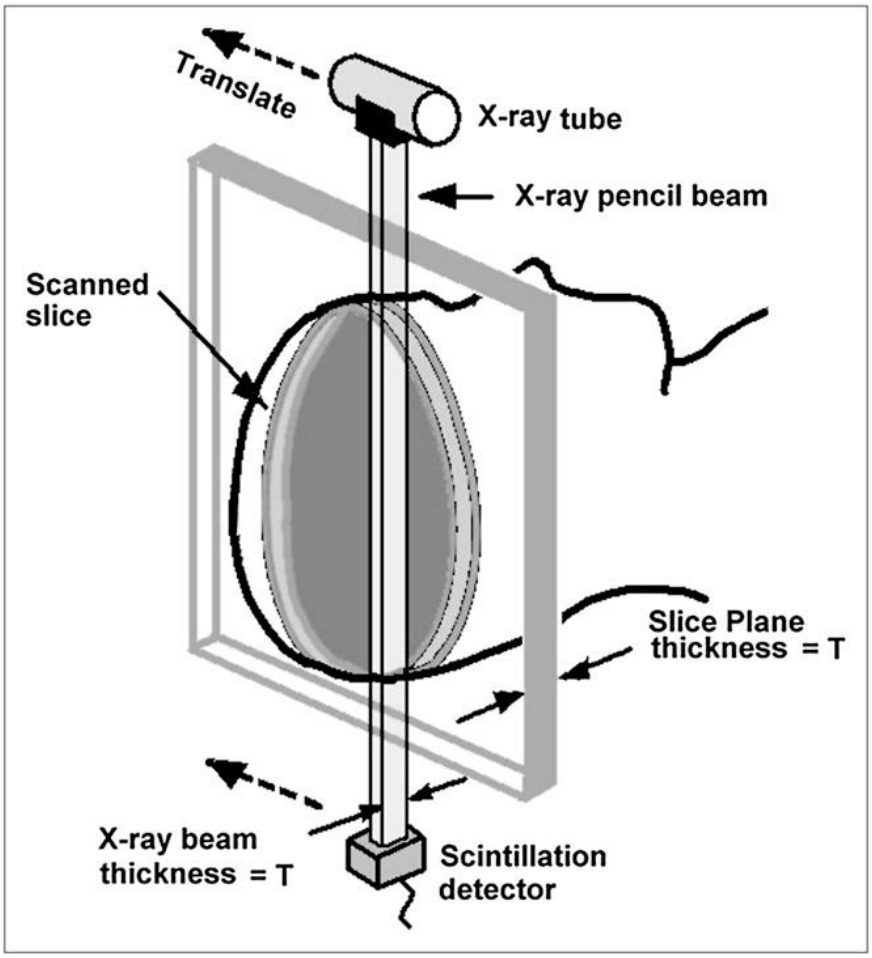

Figure 5. CT arrangement. Axial slice through patient is swept out by narrow (pencil-width) x-ray beam as linked x-ray tube–detector apparatus scans across patient in linear translation. Translations are repeated at many angles. Thickness of narrow beam is equivalent to slice thickness. (This research was originally published in JNMT. Goldman LW. Principles of CT and CT technology. J Nucl Med Technol. 2007;35:115-128. © by the Society of Nuclear Medicine and Molecular Imaging, Inc.)

5.3. Artifact types in computed tomography

Boas and Fleischmann classify CT image artifacts into a number of visual categories. [26] Their account is summarized below with the addition of details of PVE by Erlandsson et. al. [19]

First, images can have concentric bright or dark **ring artifacts** centered on and perpendicular to the scan rotation axis. They are caused by imperfect detector elements. They can be reduced by recalibration before scanning and by post-processing algorithms after scanning.

Statistical noise causes random white and dark streaks in directions of greatest attenuation (least activity). Noise artifacts can be compensated by combining data several images or by using MBIR models that add information to the image.

Beam hardening and **scatter** both manifest as dark streaks between highly attenuated regions in the image. Both phenomena are due to inappropriate increase in

detected activity, although they are caused by different mechanisms. Beam hardening is caused by higher attenuation of the low-energy part of the radiation spectrum, distorting the attenuation model by making the end section of the beam "harder" or less likely to be further attenuated by tissues. Beam scatter is apparent when photons are diverted to detectors that would have otherwise seen low activity. Beam hardening can be reduced by using a monochromatic or high energy beam, multiple scans with different energies, or by post-processing methods. Scatter is reduced by blocking photons that arrive detectors at an angle, or its effect can be estimated and subtracted at detectors, or iterative reconstruction can attempt to correct it.

PVE comprises a class of imaging resolution related artifacts that limit how well a reconstructed voxel can represent its object location. [19] The effect causes blurring at the edges of regions with different densities like demonstrated in Figure 6. There are two main factors that contribute to PVE: apparent voxel activity spill-in and spill-out caused by the imaging system transfer function, and tissue-fraction effect caused by the averaging of heterogenous activity (tissue) within a voxel, e.g. close to the edges of the scanned object. In CT context, PVE usually refers to the tissue-fraction artifacts. Its effects increase with the voxel size, and they can best be avoided by using a thin acquisition section width.

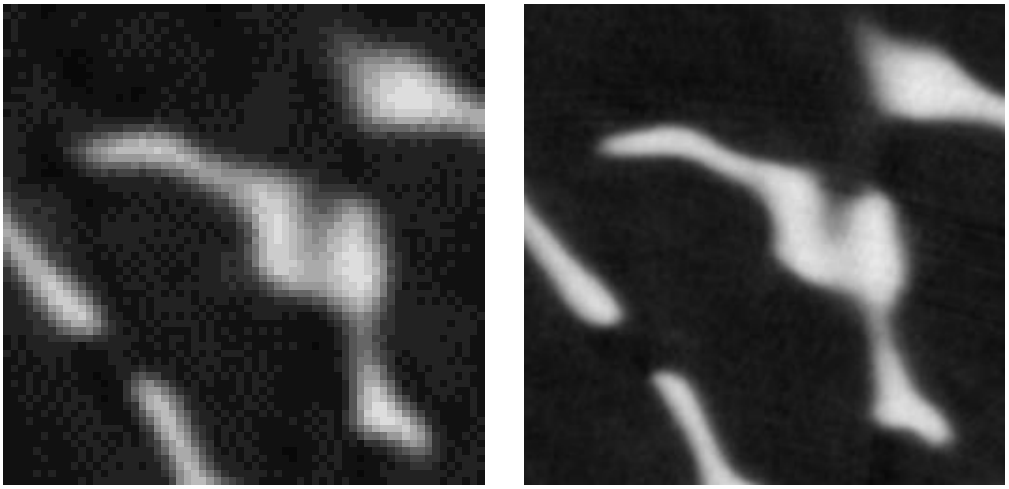

Figure 6. On the left, the reconstructed slice of sample 2 scanned at 35 μm resolution demonstrates a typical PVE-related blurring effect that occurs at tissue regions despite that trabecular bone is a high contrasts object with distinct borders. On the right, a slice from the same region scanned at 9 μm.

Motion artifacts, detected visually as blurring and double images, are caused by the movement of the scanned object during acquisition. In a broad sense, they represent a type of PVE that is dependent on the temporal instead of spatial imaging resolution.

Out-of-field artifacts appear as streaks or shading through the whole image. They arise from object regions that are outside the scanned region that cause attenuation that is not properly accounted for by the reconstruction algorithm.

Metal artifacts are caused by high attenuation regions that are out of the operational range that a scanner or reconstruction process can handle. The artifacts often appear as severe streaking, which can be reduced with specialized software.

6. MATERIALS AND METHODS

This chapter describes the utilized materials and the methodology utilized for obtaining the data. The materials comprise the scanned media, the uCT device and the software and hardware utilized for the analysis. Scanned media were cylindrical subchondral trabecular bone samples (diameter 10 mm, length 20 mm) of two bovine lateral proximal tibiae and a cylindrical 8 mm diameter thickness calibration phantom (SkyScan SP-4001, Bruker MicroCT) containing four 2 mm wide aluminum foil plates with nominal thicknesses of 20 µm, 50 µm, 125 µm and 250 µm (±10% tolerance). All samples were wrapped in foam and oriented horizontally (in proximal-distal orientation) for scanning.

We scanned the media using a µCT device (Skyscan 1172, Bruker microCT, Kontich, Belgium) set up with an Al (0.5 mm) filter, complete 360° rotation, a step size of 0.5°, and averaging of three frames. We used three camera settings: 4000 × 2672 pixels (1 × 1 binning), 2000 × 1336 pixels (2 × 2 binning), and 1000 × 668 pixels (4 × 4 binning), enabling resolutions of 8.71 µm, 17.42 µm, and 34.84 µm. These resolutions are referred to by the next highest integer sizes (9 µm, 18 µm, and 35 µm). Respective exposure time, acceleration voltage, and current settings were: 1300 ms, 50 kV, 500 µA; 350 ms, 50 kV, 500 µA; 90 ms, 40 kV, 476 µA (phantom) / 500 µA (samples). We reconstructed and analyzed the CT image stacks with manufacturer provided software (NRecon and CTAn, Bruker microCT).

We selected thresholding/segmentation volume of interest (VOI) from the middle of the scan volumes. The volumes were small enough to facilitate effective processing and large enough to produce meaningful trabecular measurements (6.7 mm x 6.7 mm x 6.7 mm).

We had access to several CT (including µCT and CBCT) image stacks of lapine, bovine, and human trabecular bone samples for testing. For the comparison of the segmentations of different modalities, we received two different scans of a cylindrical trabecular bone sample. One was a µCT scanned volume with 7 µm resolution (SkyScan 1272, Bruker MicroCT, Kontich, Belgium), and the other was a CBCT (Verity, Planmed Oy, Helsinki, Finland) scanned volume at 100 µm resolution.

The given µCT and CBCT scans were binarized with different methods (Bradley's, Otsu's) and with different parameters in effort to find matching volumes and structures. We registered both the original volumes and their segmentations manually with DataViewer (version 1.5.2.5, Bruker MicroCT) and automatically with DataViewer and MATLAB (version R2016a 64-bit, MathWorks).

We developed the automatic segmentation scripts with MATLAB and performed the automatic segmentation of the VOIs on a laptop (Fujitsu Lifebook NH532, Intel® Core™ i5-3210M CPU @ 2.50GHz with two cores, four logical processors, 16 GB RAM) using the previously selected thresholding and neighborhood parameters.

The code was managed with SourceTree front-end for Git and hosted on a free BitBucket repository[2].

[2] https://jukka_kaipala@bitbucket.org/kaipalainc/full-analysis.git

6.1. Optimization of the segmentation scripts

We used two objective quantitative criteria to make statements about the maintainability of the code resulting from our changes: cyclomatic complexity (CC) and line count statistics. We calculated the CC with MATLAB's own code checking functionality on a method level for the original, new or changed, and all MATLAB files. We used a general-purpose line counting tool (cloc v1.70, GPL v2) to extract code, blank, and comment line statistics for the same file categories, likewise on a method level.

6.2. Definition of segmentation parameters

We made two major modifications to the original segmentation method, one for the binarization step and one for the LBP-labeling step. We designed also two experimental settings to dynamically define parameter configurations, where the optimal values depend on data and modality.

Firstly, we replaced global thresholding with a new adaptive thresholding method to improve its robustness. This is a significant change that has the most potential impact on the AMLM segmentation result, since it changes the LBP-threshold.

Secondly, we added inner tissue label to the LBP-based segmentation in addition to the previously labeled outer border.

Several parameters affect segmentation. Binarization parameters (W, T, C) configure the initial volumetric thresholding, which in effect determines the segmented tissue volume. Neighborhood parameters (N_1, R_1, N_2, R_2) define the multiscale geometry for the actual LBP-based segmentation algorithm, which further segments the inner and outer object borders in the initial binary volume and relabels disconnected voxels to the background.

We estimated these two parameter sets separately, firstly because they do not have a large effect on each other, and secondly because coupling would be impractical due to large number of possible parameter combinations.

Hybrid adaptive binarization and its parameter configuration

There are several adaptive binarization methods available for MATLAB, but no method was satisfactory for our purposes, at least not out of the box. We ended up combining two fast methods that generate local threshold values by adjusting down the mean filtered image gray-values.

The first method, appropriately-named "adaptive mean thresholding", subtracts a constant value from the gray-values of mean filtered image to produce the threshold array. The second one, Bradley's method, is otherwise similar, but it downscales the mean filtered image gray-values proportionally by a fraction instead of a fixed amount.

We adapted these methods into 3D and combined them together as formulated in equation (5). The benefit of this hybrid method is that it is highly customizable. On the downside, the new method depends on three parameters:

1) Mean filter size W is the simplest parameter to configure first, because its acceptable range can be estimated from the imaged feature size and the VOI size, and it accepts only odd positive integer values.

2) The mean filtered image gray-values are usually downscaled, which means that T is positive.
3) Constant C is in practice a positive real number.

There are plausible default values for the two constituent 2D methods (with just two parameters each), but not for our hybrid method, at least not with 3D medical images. Therefore, we had to make measurements to determine credible values for the parameters. We estimated the parameters W, T, and C for the hybrid binarization method using a limited brute force approach.

We calculated the volumetric trabecular bone thickness (Tb.Th) of segmented μCT thickness phantom scans for all three resolutions using a number of different thresholding parameter sets. We ignored the least reliable measurements of plates with nominal thickness less than double the voxel size (20 μm plate at the 18 μm resolution, 20 μm and 50 μm plates at the 35 μm resolution). We calculated parameter combinations that best matched the nominal and measured phantom plate thicknesses for each resolution. We used the mean of relative (percent) plate thickness errors between the nominal and measured values as a goodness indicator. The results yielded resolution specific thresholding parameters (W, T, C) for configuring the automatic segmentation.

Configuration of the AMLM neighborhood parameters

Like with MLM, configuration of the AMLM requires four neighborhood parameters. Two parameters control the primary inner neighborhood: the number of points on the neighborhood sphere N_1, and its radius or distance from the center voxel R_1. Similarly, for the nested outer neighborhoods, one parameter, N_2, defines how close the seven neighborhood points are to each other[3], and the other parameter, R_2, sets their distance from the center voxel.

We configured the four LBP parameters by assessing SSIM between the normalized raw GT volume and segmentations of two trabecular bone samples at three different resolutions. SSIM index represents an objective measurement of visual similarity. It is based on the computation of three terms: the luminance term, the contrast term and the structural term. The overall index is a multiplicative combination of the three terms. We used the MATLAB implementation of the index calculation for volumes.

We configured AMLM to use the default (global) MLM thresholding and tested only different neighborhood parameters combinations. In addition to the default neighborhood parameter values, we set two additional alternative test values for each parameter, one slightly smaller and one larger than the default value. The inner neighborhood density N_1 was assigned arbitrary candidate value set of 18, 26 (default), and 38. The remaining parameter sets were derived from these values with rules that would produce also the default parameter combination: R_1 value set was $N_1/26$, N_2 was defined as N_1*3, and $R_2 = N_1/26+1$.

Four independent sets of three parameters resulted in $3^4 = 81$ unique parameter combinations to test. Denoting a parameter combination with $\{R_1, R_2, N_1, N_2\}$, the set of all test parameter sets was $R_1 \times R_2 \times N_1 \times N_2$, where $R_1 \in \{0.69, 1.00, 1.46\}$, $R_2 \in \{1.69, 2.00, 2.46\}$, $N_1 \in \{18, 26, 38\}$ and $N_2 \in \{54, 78, 114\}$.

[3] This parameter value stands for the number of uniformly distributed points that the umbrella-shaped neighborhood would cover if its dome were stretched into a full sphere.

We segmented all trabecular bone sample VOIs into four labels using several sets of parameters about the default values. We measured also the segmentation times.

Next, we calculated the structural SSIM index between the normalized GT volume and the segmented CT volumes to represent goodness of segmentation. We calculated linear correlations of the SSIM index with the different parameter combinations to indicate goodness of parameters. After that, we analyzed the results starting with the most correlated parameter, and selected the best set neighborhood parameters for the automatic segmentation.

6.3. Evaluation of automated adaptive binarization

The hybrid adaptive 3D thresholding method was compared to traditional user-dependent segmentation. First, the method had to be configured with our experimentally derived values for each of the three resolution settings. We performed automatic AMLM binarization on the six volumes, of the two trabecular bone samples scanned at three different resolutions, that we had already used for the configuration of neighborhood parameters.

The same volumes were binarized by two experienced users separately with CTAn (version 1.14.4.1). Both people experimented with their preferred image operations and parameters (filters, morphological, segmentation) until the results were visually acceptable, and measured the time spent on each VOI.

Next, we measured the values of structural parameters BV/TV and Tb.Th from both sets of segmented volumes with CTAn (version 1.16.4.1+ 64-bit). For GT reference, we analyzed the same parameters from the highest resolution VOIs, which we thresholded automatically (Otsu's method). We compared the measurements of the traditional user-assisted segmentation and AMLM segmentation to each other and to the GT.

Finally, we configured the 35 μm AMLM thresholding also visually with an experimental segmentation preview tool that we developed with MATLAB for this purpose. With its help, we previewed sample 1 to select a set of thresholding parameters and used them to segment both samples with AMLM.

7. RESULTS

7.1. Optimization of the segmentation scripts

Our initial task was to optimize the provided segmentation scripts and improve their robustness. We started the work by getting familiar with MATLAB, which is an established interpreted scripting language and programming environment. Its strengths lie in efficient matrix calculations, which give the language its name (MATrix LABoratory). It was designed for numerical computing but has since evolved to a full featured programming language.

Code vectorization is a MATLAB language specific speed optimization technique. It means restructuring of loop-based calculations on scalars into more efficient matrix operations on arrays (vectors).

Another language specific speed optimization technique is the possibility to compile user methods into native code, but it increases function call overhead and is not suitable for all methods.

Other common optimization techniques avoid inefficient coding patterns that waste or abuse limited resources that are either limited (RAM, graphical objects, file system) or inherently less efficient (network, file system). Preallocation of arrays is important in MATLAB, because the addition of a new element on the fly, e.g. in a loop, forces the creation of a new instance and copy the original array data. Method inlining eliminates calling overhead and is also an efficient speed optimization technique with frequently called local methods.

These are only general speed optimization guidelines. In practice, optimization requires extensive profiling experimentation with different alternative solutions, as well as taking care to keep the code modular and maintainable. For this reason, we took care to follow recommended MATLAB coding conventions[4] where the guidelines were not in full conflict with the original coding style.

As an early version, the scripts were written for functionality and had not been optimized yet. Segmentation speed was an obvious target for improvement. Inefficient memory use presented another problem, because it limited the size of volumes that could be segmented in addition to hindering the performance of the method.

Maintainability

We adapted the original main script into a self-contained method, so that it could be easily called from other methods. We modularized much of the code into nested functions to control individual method sizes. Configuration constants for segmentation and testing were placed in a separate class.

The extracted code statistics, summarized below in Table 1, show that the new and edited script files contain proportionally more blank and comment lines than the original code. Moreover, the final scripts have much lower mean and median CC on the method level.

The final scripts have also about 60% more lines of code compared to the original. Most of the new functionality consists of the binarization module and its support methods (user interface, file I/O, test/debug, parameters). The new code was generally structured and documented to facilitate code maintenance.

[4] https://se.mathworks.com/matlabcentral/fileexchange/46056-matlab-style-guidelines-2-0

Table 1. Comparison of code characteristics of the original and final scripts

File category	File count	Total lines	Code lines	Blank lines	Comment lines	Code/total lines ratio (%)	Avg. CC	Median CC
Original	55	7820	4923	1868	1029	63.0	17.3	12.0
Final/all	80	14745	8008	2869	3868	54.3	9.4	6.0
Edited	35	6662	3013	1018	2631	45.2	6.2	3.5

Performance

We explored the coding style and functionality by stepping through the code while running the scripts on the provided image stacks. We used the profiling and debugging tools of MATLAB to locate performance bottlenecks in the code on function and statement level. We profiled the code by segmenting lapine trabecular bone image stacks that were the built-in source material for the original scripts.

The profiler indicated that performance bottlenecks were related to file I/O (mask and data stacks), inefficient memory management (preallocation and release), and vectorizable scalar loops. Data structures were regularly validated against the original intermediate results using test functions during development. Table 2 shows that the optimized scripts allocated less memory and outperformed the original version, even though the optimized script includes the performance impact of local thresholding in LBP-based segmentation. This configuration does exclude the effects of local binarization and the additional border label.

Table 2. Performance comparison of the original and optimized scripts

Run state	Script version	Allocated (GiB)	Freed (GiB)	Peak memory usage (GiB)	File I/O time (s)	Other processing time (s)	Total execution time (s)
Clean	Original	14.38	6.55	2.61	60	279	338
	Optimized	6.04	5.98	2.61	48	38	86
Rerun	Original	14.38	14.39	2.61	52	161	213
	Optimized	5.95	5.94	2.61	47	31	78
	Skeleton[5]	5.30	5.29	2.61	5	27	32

All values are averages of three measurements. Run state ‘clean’ stands for initial segmentations in a freshly loaded MATLAB 2016a development environment, and ‘rerun’ stands for any subsequent runs. The run state has a large effect on the original script performance. Time and memory usage is as reported by the MATLAB profiler.

We estimated the effect of our additional AMLM border label on the segmentation speed separately. In this experiment, we segmented our two bovine trabecular bone volumes using both label configurations. Table 3 summarizes our results.

[5] Static VOIs, empty frames not written.

Table 3. Performance impact of the additional AMLM label

Sample, resolution	Segmentation time, 3 labels (s)	Segmentation time, 4 labels (s)	Segmentation time increase (%)
1, 9 µm	342	404	18
1, 18 µm	56	63	13
1, 35 µm	6	8	33
2, 9 µm	354	397	12
2, 18 µm	56	60	7
2, 35 µm	6	7	17
Combined total	820	939	15

Note that the low-resolution volumes are segmented in a few seconds, and their time increase percentages are not reliable at this measuring accuracy.

7.2. Definition of segmentation parameters

First, we scanned the two subchondral trabecular bone samples of bovine tibia in three resolutions. We post-processed reconstructed volumes to reduce noise, ring artifacts and beam hardening artifacts.

Binarization parameters

We selected a thickness phantom with four aluminum foils, with nominal thickness values comparable to the trabeculae of the samples we were going to scan. We scanned the phantom in three resolutions that we were going to use for scanning our actual samples.

Next, we picked plausible initial parameters visually for the best resolution, selected a number parameter sets about the initial values, and separately segmented each foil of the phantom VOI with all parameter sets.

We measured the mean volumetric Tb.Th of the segmented phantom foils for each parameter set and selected the one (parameter set) with the smallest mean relative error, where nominal foil thickness is assumed to be the actual thickness.

Lower resolutions required more iterations of the same principle, although we were able (or forced) to fix the window size value for the other two. Due to the low resolution, there were fewer foil widths to measure, which made evaluation of parameters more unreliable. For this reason, we constructed a visual configuration tool to assist with the configuration of parameters for the 18 µm and 35 µm resolutions. Figure 7 shows a sample screenshot of the tool. With it, we could adjust a group of multiple parameter combinations on the fly. More importantly, we were able to visually compare their effects on the binarization of a volume and quickly eliminate parameter combinations that simply did not work out.

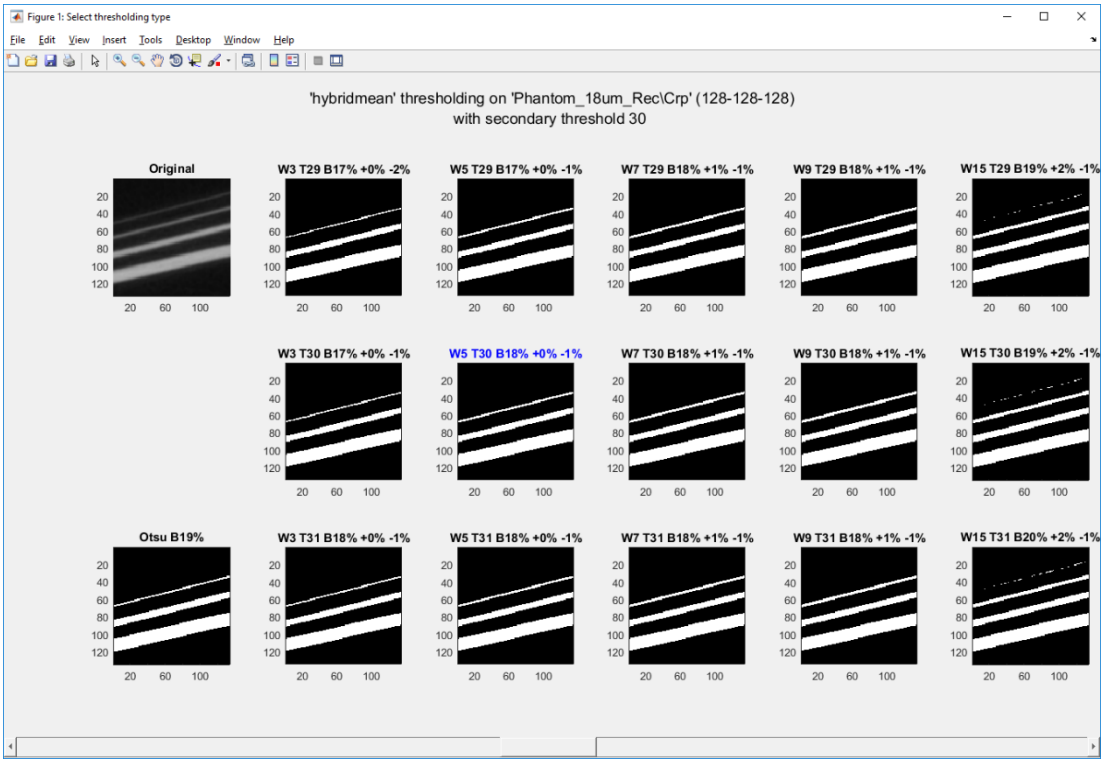

Figure 7. Screenshot of the interactive binarization preview tool. The viewing direction is limited XY- and WT-planes, but the view may be moved freely in the image stack and configuration space. The top left image represents the original volume and the bottom left image the default binarization (Otsu's method) for reference.

We selected the thresholding parameter values in Table 4 for each resolution based on the measurements of phantom scans segmented with different parameters.

Table 4. Selected thresholding parameters for each resolution based on segmented phantom scan measurements. W (px) = mean filter kernel size; T (%) = mean image downscaling adjustment; C*256 = downscaled mean image absolute adjustment as normalized fraction value multiplied by 256; μ_δ (%) = mean percent error from the nominal phantom plate thickness

Resolution	*W* (px)	*T* (%)	*C**256	μ_δ (%)
9 µm (4 plates)	7	17	18	2.951
18 µm (3 plates)	5	30	30	2.492
35 µm (2 plates)	3	40	60	7.072

Note the relatively large mean percent error between the Tb.Th measured from the binarized foil segmentation and its nominal thickness at the lowest resolution. As illustrated in the following graphs, in Figure 8 through to Figure 11, segmented foil thickness is sensitive to small parameter value changes when nominal foil thickness

(20 µm as opposed to 250 µm) is relatively close the nominal resolution, even if the resolution is high (9 µm).

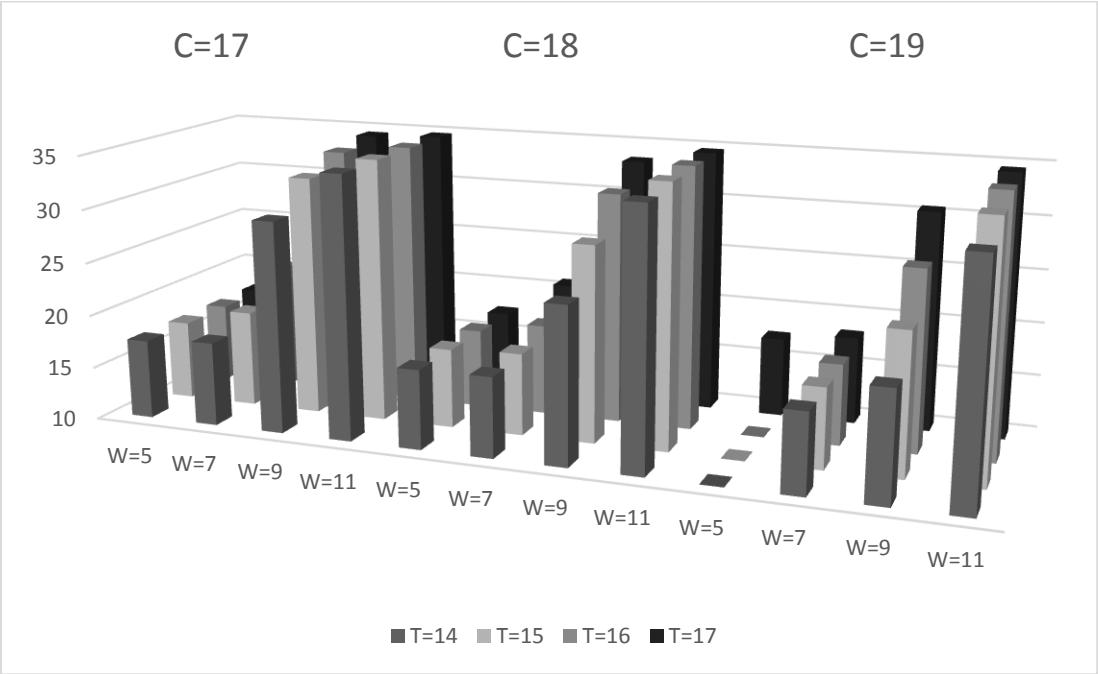

Figure 8. Measured Tb.Th of 20 µm (left) and 250 µm (right) foils segmented from 9 µm volumes with different values of *W, T, C*.

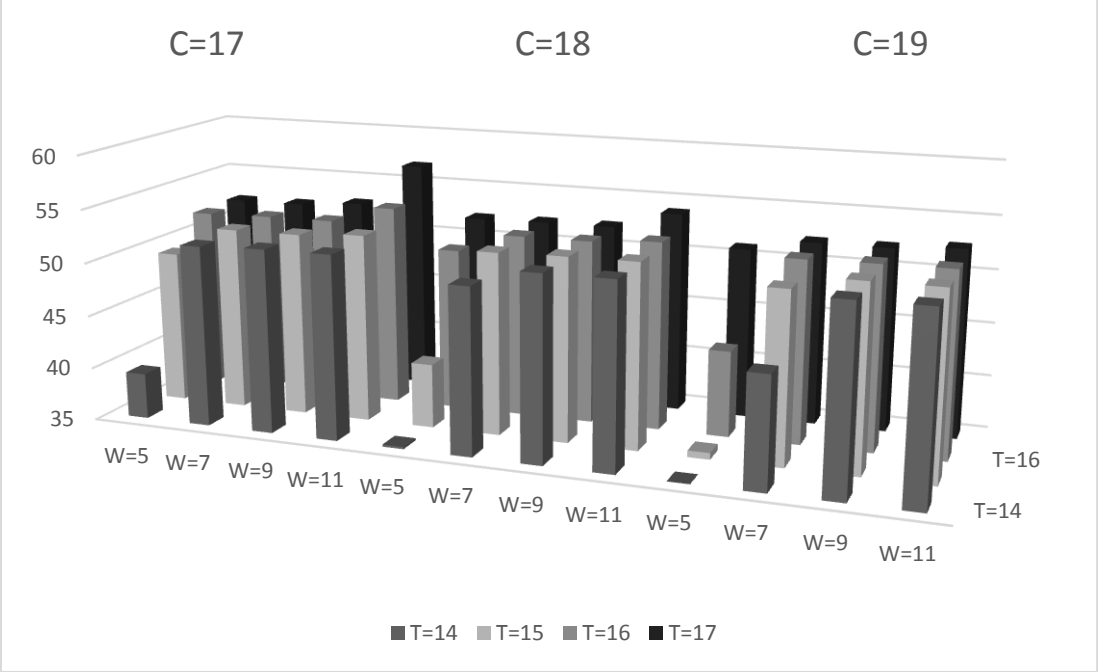

Figure 9. Measured Tb.Th of 50 µm foils segmented from 9 µm volumes with different values of *W, T, C*.

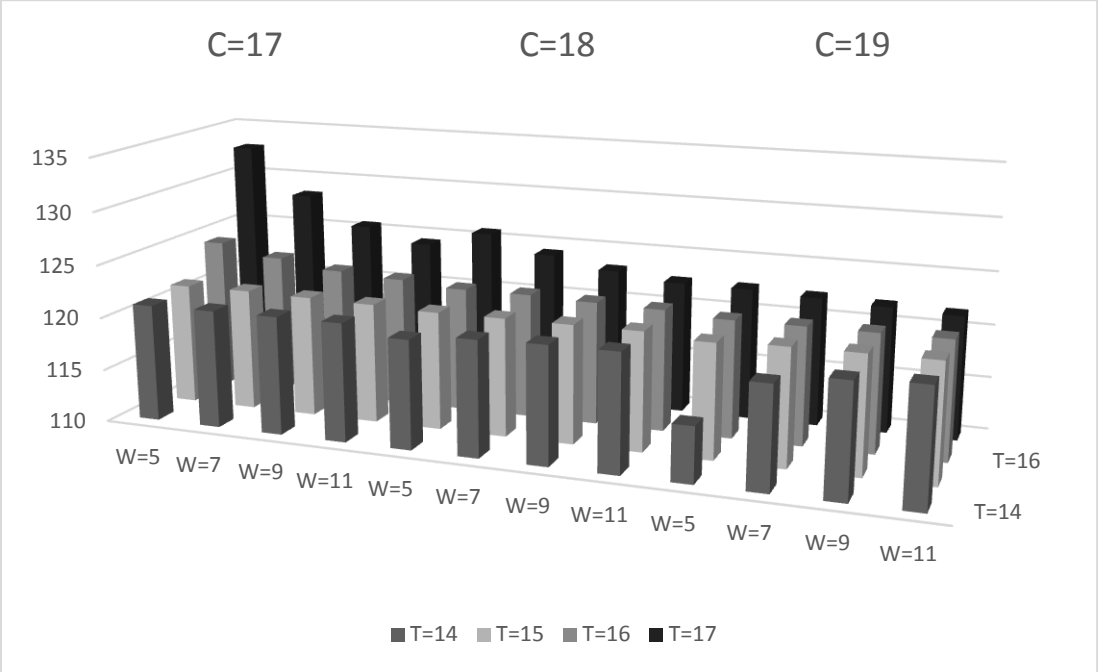

Figure 10. Measured Tb.Th of 125 µm foils segmented from 9 µm volumes with different values of *W, T, C*.

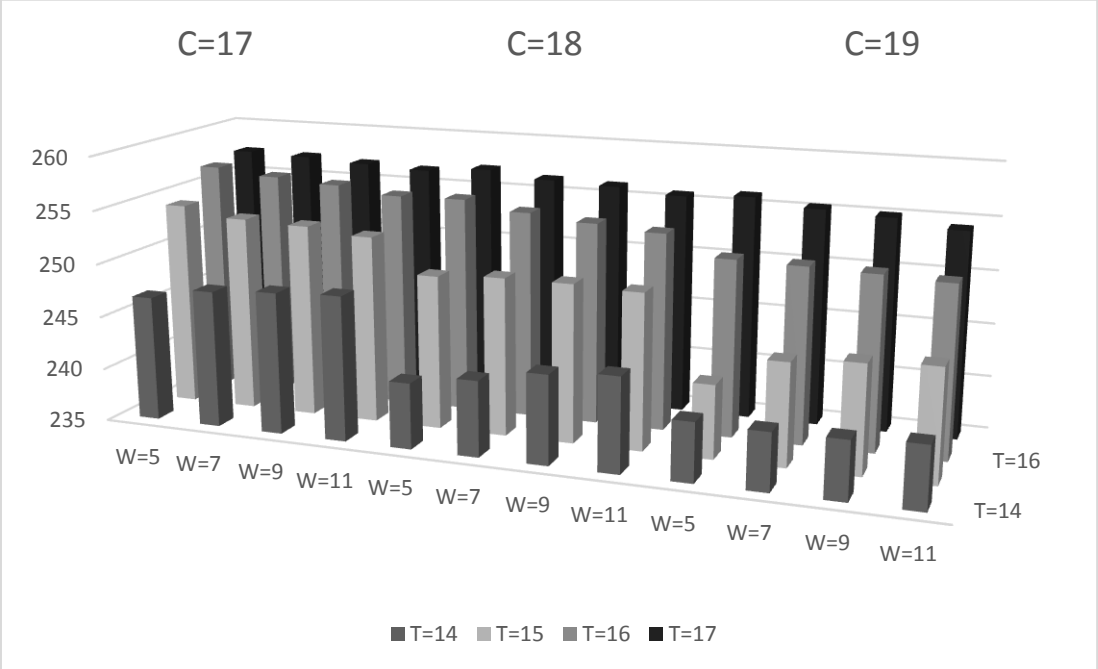

Figure 11. Measured Tb.Th of 125 µm foils segmented from 9 µm volumes with different values of W, T, C.

Comparison of the thickness profiles underlines the more chaotic nature of the PVE-dominated segmentation of small features with respect to small parameter value changes.

Neighborhood parameters

We segmented the VOI at three resolutions using all parameter combinations and calculated their SSIM with the GT. We determined sample correlation coefficients μ_r between the parameter values and corresponding SSIM index and thresholding time, and averaged them over the VOIs in Table 5. The results show that both SSIM and segmentation time express the strongest linear dependency on the inner neighborhood radius parameter R_1.

Table 5. Average sample correlation coefficients μ_r of the tested neighborhood parameter values with similarity and segmentation time; constant values are R_1 = 1.46 and N_1 = 38; SD = standard deviation

Constant parameter	Correlated parameter	SSIM		Segmentation time	
		μ_r	SD	μ_r	SD
-	R_1	0.996742300	0.000789079	0.870272193	0.012790265
	N_1	0.055986465	0.002272591	0.170243243	0.063093335
	R_2	-0.003343024	0.000537735	0.007627258	0.038023432
	N_2	0.000336614	0.001993851	-0.030461281	0.005478575
R_1	N_1	0.912460769	0.011077648	0.826272783	0.041962928
	R_2	-0.031314714	0.045380142	0.053173526	0.121071452
	N_2	0.047020701	0.053080101	-0.105909680	0.013584591
R_1, N_1	R_2	-0.003343024	0.000537735	0.007627258	0.038023432
	N_2	0.000336614	0.001993851	-0.030461281	0.005478575

Keeping the inner radius R_1 constant with the parameter value that gives the greatest similarity, the next set of averaged correlations show that N_1 is the next relevant parameter whose value correlates with SSIM. Measurements of the remaining parameters R_2 and N_2 do not significantly correlate with SSIM when the more significant parameters R_1 and N_1 were set constant with values that maximized their contribution to SSIM. However, the data in Figure 5 show that segmentation with the default outer neighborhood radius R_2 = 2 was interestingly about 6% faster than segmentation using either higher or lower R_2 value.

Based on these results, we selected the neighborhood parameter values for automatic segmentation as R_1 = 1.46 (=38/26), N_1 = 38, R_2 = 2, and N_2 = 78.

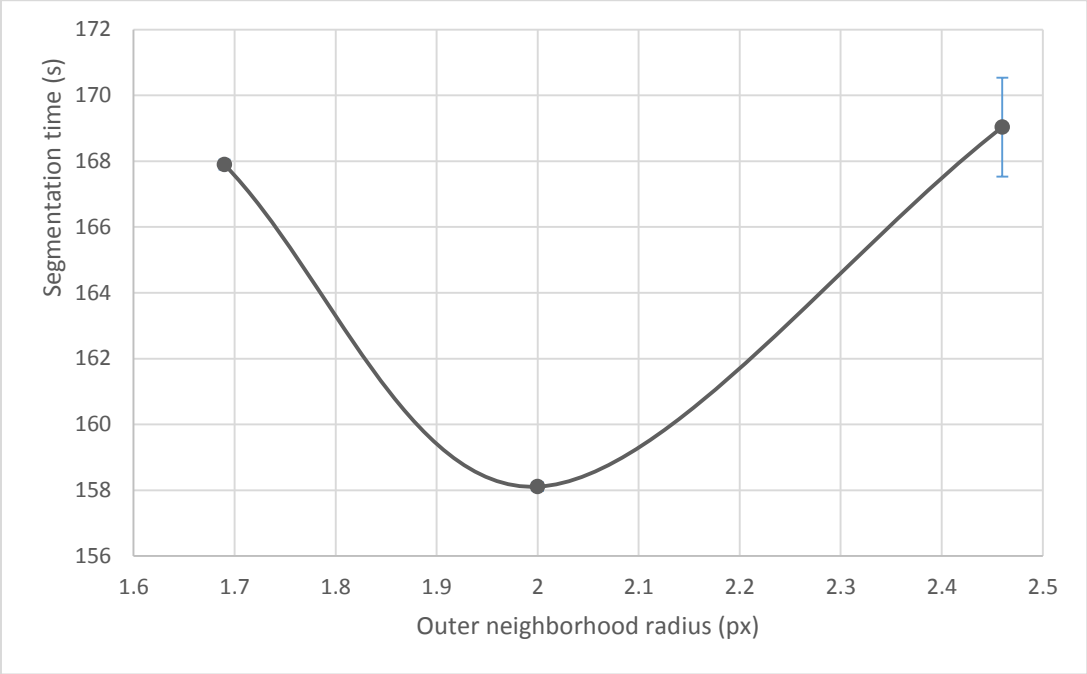

Figure 12. Dependency between average segmentation time and outer neighborhood radius R_2 with $R_1 = 1.46$ and $N_1 = 38$.

7.3. Evaluation of automated adaptive binarization

We binarized the two samples again using the estimated parameters values. For comparison, we had the same VOIs binarized also by two experienced users using their preferred methods.

The AMLM segmentation was performed using the previously selected thresholding and neighborhood parameters. Meaningful analysis requires parameters that indicate trabecular bone quality and can be compared to our other measurements. We therefore measured two common trabecular bone structural parameters, BV/TV and Tb.Th. See example with CTAn screenshot in Figure 13.

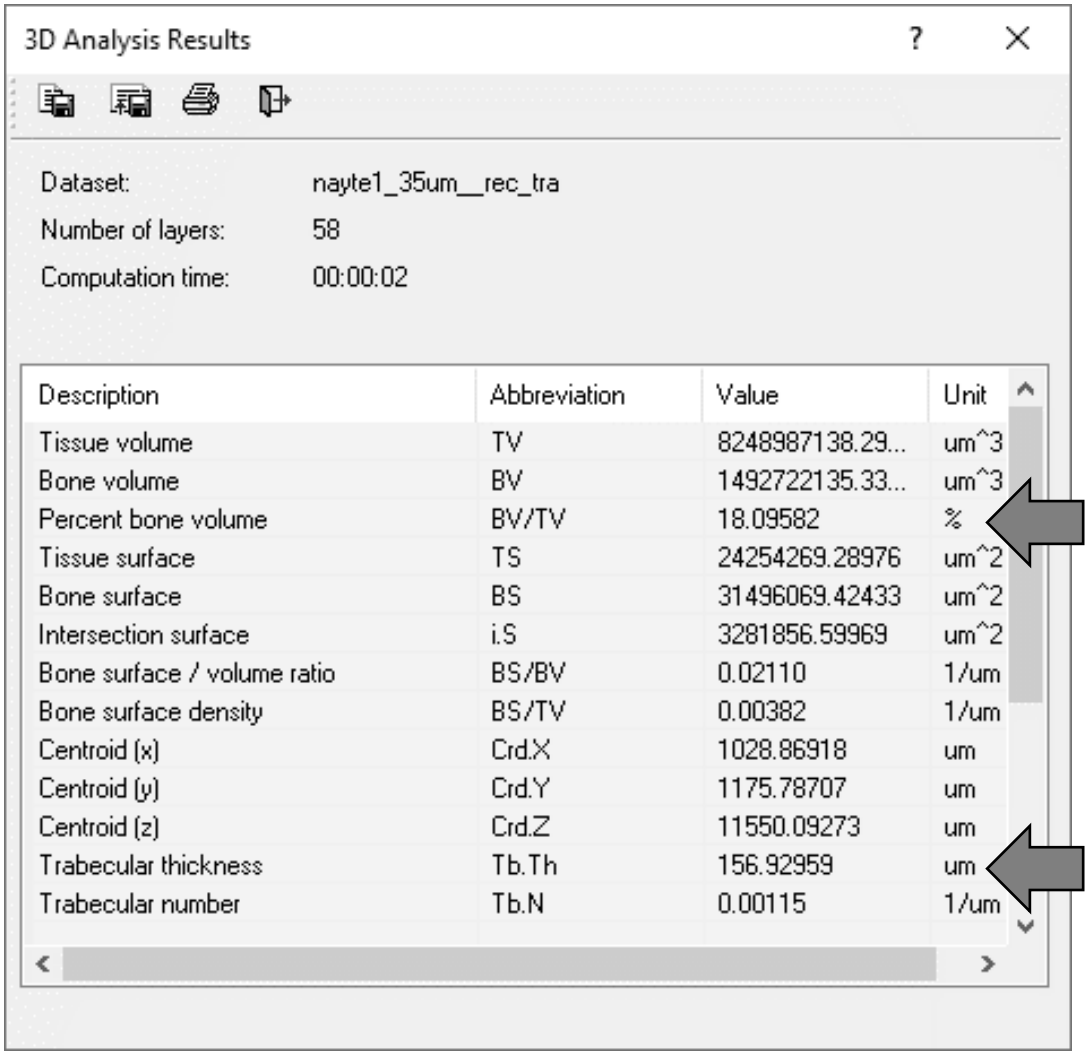

Figure 13. CTAn provided trabecular parameters for sample 1, resolution 35 µm. The arrows to the right indicate BV/TV and Tb.Th values on the third and twelfth data rows respectively.

Binary thresholding and complete trabecular border segmentation times were also included, as shown in Table 6. The data include measurements using the alternate visual setup for the 35 µm volumes, as well as the GT reference measurements. The 35 µm resolution BV/TV and Tb.Th measurements of the original AMLM configuration are markedly different from the other measurements. Binarization times are very small compared to trabecular segmentation times.

Table 6 shows also measurements from volumes that were segmented with alternative parameters. These parameter values were derived visually for the low-resolution scan, because the parameters were difficult to nail down with objective measurements and numerical methods.

Table 6. Measurements from AMLM segmentation results except where indicated; * = Automatic Otsu's thresholding of the best resolution (that is, GT); ** = Binarized using the alternative thresholding parameters ($W = 3$, $T = 53$, $C = 60$)

Sample, resolution	BV/TV (%)	Tb.Th (μm)	Binarization time (s)	Segmentation total time (s)
1, 9 μm	23.22052	184.70	2	404
1, 9 μm *	21.42417	180.18	n/a	n/a
1, 18 μm	24.30018	193.43	1	63
1, 35 μm	18.09582	156.93	0	8
1, 35 μm **	24.34506	190.31	0	n/a
2, 9 μm	15.78273	205.81	1	397
2, 9 μm *	14.39293	201.80	n/a	n/a
2, 18 μm	16.25249	210.43	0	60
2, 35 μm	11.60439	176.42	0	7
2, 35 μm **	12.53121	208.24	0	n/a

We measured the BV/TV and Tb.Th of the traditionally binarized volumes as reference for comparison with the automatic segmentation as shown in Table 7. Segmentation takes several minutes, and time deviation is large. Measured BV/TV and Tb.Th values tend to be greater at lower resolutions.

Finally, we measured the volumetric trabecular thickness of all binarizations, as well as the GT for reference. Measurements from automatic segmentation were closer to GT. Measurement of bone volume percentage yielded similar results as expected, although they were slightly less pronounced.

Table 7. Average measures from traditional binary segmentation; SD = standard deviation

Sample, resolution	BV/TV (%)	SD	Tb.Th (μm)	SD	Binarization time (s)	SD
1, 9 μm	24.6	1.62	201	10.7	573	216
1, 18 μm	24.7	3.52	204	22.2	227	66
1, 35 μm	27.1	2.26	237	1.98	1069	694
2, 9 μm	16.8	1.06	222	9.25	562	308
2, 18 μm	17.1	1.41	225	13.0	355	177
2, 35 μm	18.3	1.26	243	9.41	366	93

Comparison of automatic AMLM segmentation results to traditional segmentation in Figure 14 shows that the bone structural parameter measurements from AMLM are slightly lower but comparable to traditional segmentation, with percent ratios over 90%. The measures taken from the lowest resolution VOIs are significantly lower, with percent ratios mostly below 70%.

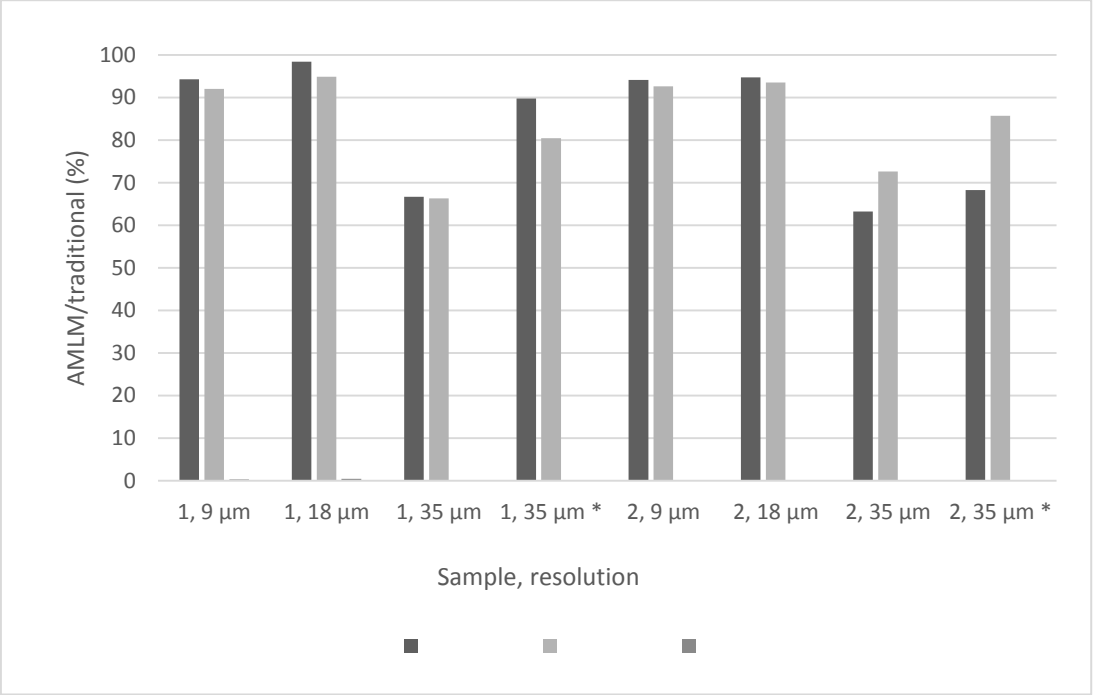

Figure 14. Percent ratio of the automatic and traditional segmentation measurements for different VOIs (sample, resolution). * = Segmented using the alternative AMLM thresholding parameters.

We compared also the automatic adaptive binarization speed to traditional user-assisted binarization, although the binarization time bars are difficult to make out in the figure. There is some variability in the data, but automatic binarization takes less than half a percent of the traditional binarization time in every case. Binarization time with the parameterized 3D hybrid method is negligible compared to traditional thresholding even at the highest resolution, where the VOI consists of 256^3 or 16,777,216 voxels.

Figure 15 compares measured structural parameters of both AMLM and traditional segmentation to those of the best resolution VOIs (that is, GT). All measurements from AMLM segmented VOIs are closer to the GT than traditionally measured values.

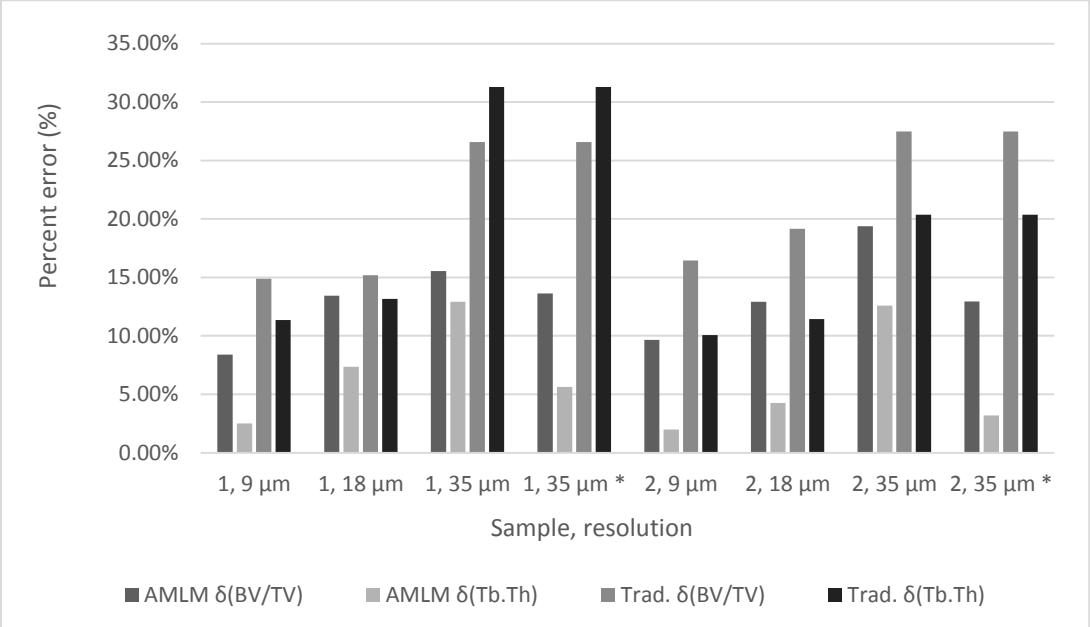

Figure 15. Percent error of the automatic and traditional segmentation measurements compared to the best resolution raw image measurements. * = Segmented using the alternative AMLM thresholding parameters.

7.4. Assessment of the effects of image resolution and artifacts

The scanner was set up to reduced certain artifacts automatically (noise, beam hardening). PVE caused the most severe detected artifacts, especially in low-resolution scans. Noise was reduced both by the scanner software and during reconstruction. Some motion artifact was detected, which was eliminated with a rescan. Beam hardening, scatter, and ring artifacts were present, and we reduced their effects in the reconstruction process. There were no metal artifacts. Overall, the image quality was very high.

7.5. Comparison of segmented data from different modalities

We could not get meaningful results from comparisons of reconstructed µCT and CBCT volumes of the same trabecular bone sample. The volumes did not have any markers to simplify registration. It was possible to reduce the degrees of freedom to two (z-rotation, z-position) because of the shape of the sample and known scaling factors, but neither automatic nor manual registration could be performed confidently, whether on raw of segmented volumes. For this reason and also due to the lack of further available samples, the comparison with CBCT was not feasible.

8. DISCUSSION

Our overall purpose in this work was to further the CT-based study of bone and joint diseases by continuing the development of a novel specialized trabecular bone segmentation method.

Our preliminary objective was to **improve the performance of the segmentation scripts**. The main goals of this work were to **extend the automatic segmentation method** with adaptive thresholding and additional label, to define sample and modality specific **segmentation parameters**, and to assess the modified method by **comparing automated binarization results to traditional user-assisted binarization**. Additionally, we assessed the effects of **image resolution and artifacts**, and compared segmented data between **µCT and CBCT**.

Optimization of the segmentation scripts

Overall, the evidence suggests that we succeeded in improving the performance of the segmentation script and made a visible effort to limit maintainability issues while optimizing the existing code and writing new features. Also, optimization needs had to be compromised with those of maintainability, because they required opposite design patterns.

Maintainability

The new script contains significantly more comment lines than the original, which is a weak indicator of better readability and maintainability of the code. It is difficult to interpret as a positive indicator based on mere statistics, because verbose commenting does not necessarily improve readability and maintainability. Nevertheless, many of our code comments describe the purpose and syntax of methods as recommended in MATLAB style guidelines. Other comments clarify the logic and function of more complex statements and blocks of code. For example, highly vectorized code is often less readable than corresponding scalar loop structure.

However, the new script contains also many more code lines (+60%). The size of the code base is directly related with how difficult the management is and the number of programming bugs that it is likely to hide. Then again, part of the increase results from our coding style preference of short lines over short code blocks compared to the original style.

Performance

The new scripts have at least 50% smaller average CC on the method level, which suggests that we did improve the maintainability of the original code base. CC is controversial as a sole meter of quality code, but it is still an objectively measurable code property. Moreover, the findings agree with our tentative interpretation of the code line statistics. Also, we adhered consciously to the accepted MATLAB coding conventions during the project, and managed and documented our edits with the source code control system. Although these are not quantifiable facts, they add some confidence to positive claims about the results of the coding process.

Performance data indicate that the optimized segmentation script runs up to about seven times (400-700%) faster than the original code. Improvement depends on the

configured optimization level. The new segmentation features, i.e. local thresholding and additional border label, have a relatively small negative effect (about 5 percentage points) to this performance improvement. The negative performance impact is small in our setting, although the results suggest that it increases with the volume size and further depends on the characteristics of the volume data.

The memory report data shows that the optimized script allocates less than half of the original amount of memory. This makes it more memory efficient, which is also a speed factor in MATLAB. There is a caveat though, because the memory report feature is unsupported and undocumented, even though it has been widely used in the MATLAB community for years.

Extensions to the LBP-based segmentation method

Like expected, the additional fourth segmentation label inevitably increases segmentation time. The increase about 15% compared to three-label segmentation of the trabecular bone samples used in this project. The performance impact is not critical, especially when considering that the original unoptimized method used hundreds of percent more time for segmentation.

We hypothesize that our additional label and neighborhood parameter adjustments could improve the segmentation results for subsequent analysis of the trabecular bone microstructure. However, we did not investigate how the label would have affected the LBP-based structural analysis of the segmentation results. The assessment of the effect would have required comparative structural analysis, which was outside of the scope of this work.

Estimation of thresholding parameters

We were able to select thresholding parameters using our approach, but the process was time consuming and difficult to automate. A drawback of the new adaptive local thresholding is that it requires three external thresholding parameters. Optimal parameter values cannot be based on simple rules, and they must be determined experimentally for each tissue, imaging modality, and resolution, for example with a thickness phantom like here. Even then, parameter configuration takes time and the manual process is prone to inaccuracies, especially at low resolutions, which undermines the repeatability of automated segmentation.

The configuration of thresholding parameters can be made easier and more reliable with an interactive thresholding preview tool, which facilitates experimenting with different parameters starting with reasonable default values. We developed such tool and used it to configure alternative thresholding parameters for the lowest resolution. The results show improved similarity with GT. The configuration tool also made the configuration process subjectively easier, faster, and more reliable. Although anecdotal, the improved results are encouraging, and it seems possible that a visual tool could help with the parameterization.

The thresholding parameter estimates were expected to be less reliable at lower resolutions due to lower image quality and smaller number of phantom foils whose thickness could be measured. The large mean percent error at the lowest resolution is therefore not surprising. We think that a more reliable automated configuration must be based on additional information about the experimental setting, e.g. the μCT parameters.

Adjustment of neighborhood parameters

We were able to find reasonable set of neighborhood parameters using our method. It was possible to automate the mechanical and repetitive segmentation and similarity analysis process with MATLAB scripts. In retrospect, we could have analyzed even larger number of parameters sets without serious problems.

The first trabecular bone sample for this experiment had to be rescanned because it of slight blurring that could not be compensated during post-processing. We assume that the refrigerated sample had not had enough time to adjust to ambient temperature and humidity, which caused a motion artifact as the sample heated during the initial scan.

The calculated correlation coefficient results show that both SSIM and segmentation time express the strongest linear dependency on the inner neighborhood radius parameter R_1 and to a lesser degree with the corresponding count of points N_1. The outer neighborhood parameters did not express significant linearity with measurements, but outer neighborhood radius $R_2 = 2$ interestingly resulted in faster segmentation than either larger or smaller value. We believe that the smaller radius increases the likelihood of algorithmic conditions that lead to slightly more operations. With radii $R_1 = 1.46$ and $R_2 = 1.69$, the inner and outer neighborhoods are very close to each other, well within a voxel region. Therefore, points are more likely to be classified the same way, which makes the algorithm evaluate more points before it concludes. On the other hand, the largest outer radius value $R_2 = 2.46$ increases the size of calculation arrays, because the outer neighborhood regions cover larger (voxel) block volume as the value of R_2 crosses the integer border (here 2), making operations more expensive.

Comparison of automatic and manual binarization

According to the results, all AMLM binarized volumes had a quality edge over traditional user-assisted binarization. All measurements of structural parameters from AMLM binarized VOIs were closer to our GT than the traditionally binarized volumes. This was true especially for the measurements of Tb.Th, which is not surprising, because the AMLM binarization was parameterized with thickness measurements.

We compared also the speed of automated AMLM binarization to traditional user-assisted binarization. The automatic binarization took less than half a percent of the traditional method time in every case. The automatic method was clearly faster with these resolutions and volumes of interest. Note though, that this performance measurement does not account for the time spent on the configuration of segmentation parameters. Then again, we envision that it would be eventually possible to pick parameters that have previously produced good results in similar experimental setups.

The new adaptive thresholding method turned out to be both fast and accurate compared to traditional user-assisted segmentation. Nevertheless, further testing is needed to confirm our hypothesis in more extensive experiments, especially comparative analysis of the segmented bone microstructure using data produced with different segmentation methods.

Assessment of the effects of image resolution and artifacts

The μCT scanned samples of high quality and relatively free of artifacts. The effects of noise and tissue-fraction PVE became significant with the experimental configuration of binarization parameters, especially when analyzing low resolution volumes that contained small or low contrast features.

Comparison of segmented data between different modalities

Different imaging modalities were not considered, because we failed to get meaningful results from comparisons of reconstructed μCT and CBCT volumes of the same trabecular bone sample. The resolution difference was great, but the biggest problem was that the CBCT image resolution was simply too low for extracting information from the sample. Judging by visual comparison to the μCT volume, the raw CBCT volume featured more noise and PVE than trabecular structure.

Recommendations

The hybrid binarization method that we added to AMLM performs well once configured. In practice, the time required to configure the method can be significant and must be considered in a new setting. If there are only a few segmentations to make, the portion of time spent on configuration will dominate, which may be unacceptable unless justified by the objective automated segmentation. We recommend further investigation of the visual configuration tool to simplify the estimation of parameters. The configuration of thresholding parameters can be made easier and more reliable with an interactive thresholding preview tool, which facilitates experimenting with different parameters starting with reasonable default values. Further experiment should be conducted to eventually link the μCT parameters and the thresholding parameters to reach a fully automatic protocol.

Suggestions for additional research

As future work, the segmentation method could be tested with more varied data to determine how our results are able to generalize and to which extent they depend on the characteristics of the data. Also, the performance of the AMLM compared to the original method remains to be evaluated in statistical bone microstructure analysis. The 3D thresholding method might find use in other applications where speed or computational simplicity is important.

9. CONCLUSION

In this study, we modified the multiscale LBP-based segmentation method with adaptive binarization, additional label, and dynamic configuration of parameters. We have demonstrated a successful application of the generalization of the adaptive mean thresholding and Bradley's method in 3D as part of the segmentation. To our knowledge, neither of these thresholding methods has been adapted into 3D and applied to analysis of medical images before.

We have shown how neighborhood parameter adjustment affects the perceived similarity of the segmentation result to the source volume and suggested more optimal values based on the results.

We compared the automatic method to the traditional segmentation performed by two experienced users. The automatic method outperformed traditional segmentation in binarization speed by being about two hundred times faster in the worst case, and its relative BV/TV and Tb.Th measurement errors were respectively 33% and 57% smaller on the average. This indicates that the method was successful for the used equipment and samples. However, the varied Tb.Th measurement results indicate that the automatic segmentation method configuration is not reliable at low resolutions. Corresponding measurements of low-resolution VOI segmentation configured visually with adaptive thresholding tool are more in line with the other measurements, and further suggest that thresholding parameter configuration is a problem.

We selected the hybrid adaptive mean thresholding method, because neither Bradley's method nor Adaptive mean thresholding could produce generally satisfactory results by themselves, and mean filter was preferred over median and Gaussian filters because of its superior speed performance in this setting. This was also the reason why more sophisticated segmentation methods were rejected. However, these considerations will change if more efficient methods become available, or if computation power and memory become significantly less of a factor in the future.

The new binarization method was more reliable, which is no wonder since it is deterministic, but it was also faster and more accurate than traditional user-assisted segmentation. However, its initial configuration is a time-consuming process with this approach, even if parameters are set only once for each setting. Moreover, there is no guarantee that the results would always be optimal. More work is needed to streamline the adaptive method configuration.

10. REFERENCES

[1] Kaipala J, Bordallo López M, Saarakkala S & Thevenot J (2017) Automatic segmentation of bone tissue from computed tomography using a volumetric local binary patterns based method. In: Sharma P & Bianchi FM (eds) Image Analysis 10270. Cham, Springer International Publishing: 221–232. DOI: https://doi.org/10.1007/978-3-319-59129-2_19.

[2] McAlindon TE, Bannuru RR, Sullivan MC, Arden NK, Berenbaum F, Bierma-Zeinstra SM, Hawker GA, Henrotin Y, Hunter DJ, Kawaguchi H, Kwoh K, Lohmander S, Rannou F, Roos EM & Underwood M (2014) OARSI guidelines for the non-surgical management of knee osteoarthritis. Osteoarthritis and Cartilage 22(3): 363–388. DOI: https://doi.org/10.1016/j.joca.2014.01.003.

[3] Kerckhofs G, Sainz J, Maréchal M, Wevers M, Van de Putte T, Geris L & Schrooten J (2014) Contrast-enhanced nanofocus x-ray computed tomography allows virtual three-dimensional histopathology and morphometric analysis of osteoarthritis in small animal models. CARTILAGE 5(1): 55–65. DOI: https://doi.org/10.1177/1947603513501175.

[4] Chu CR, Williams AA, Coyle CH & Bowers ME (2012) Early diagnosis to enable early treatment of pre-osteoarthritis. Arthritis Research & Therapy 14: 212. DOI: https://doi.org/10.1186/ar3845.

[5] Pap T & Korb-Pap A (2015) Cartilage damage in osteoarthritis and rheumatoid arthritis - Two unequal siblings. Nature Reviews Rheumatology 11(10): 606–615. DOI: https://doi.org/10.1038/nrrheum.2015.95.

[6] Bolbos RI, Zuo J, Banerjee S, Link TM, Benjamin Ma C, Li X & Majumdar S (2008) Relationship between trabecular bone structure and articular cartilage morphology and relaxation times in early OA of the knee joint using parallel MRI at 3T. Osteoarthritis and Cartilage 16(10): 1150–1159. DOI: https://doi.org/10.1016/j.joca.2008.02.018.

[7] Burr DB & Gallant MA (2012) Bone remodelling in osteoarthritis. Nature Reviews Rheumatology 8(11): 665–673. DOI: https://doi.org/10.1038/nrrheum.2012.130.

[8] Burghardt AJ, Link TM & Majumdar S (2011) High-resolution computed tomography for clinical imaging of bone microarchitecture. Clinical Orthopaedics and Related Research® 469(8): 2179–2193. DOI: https://doi.org/10.1007/s11999-010-1766-x.

[9] Finnilä MAJ, Thevenot J, Aho O-M, Tiitu V, Rautiainen J, Kauppinen S, Nieminen MT, Pritzker K, Valkealahti M, Lehenkari P & Saarakkala S (2017) Association between subchondral bone structure and osteoarthritis

histopathological grade. Journal of Orthopaedic Research 35(4): 785–792. DOI: https://doi.org/10.1002/jor.23312.

[10] Thevenot J, Hirvasniemi J, Finnilä M, Lehenkari P & Saarakkala S (2018) Volumetric assessment of bone microstructures by a 3D local binary patterns –based method: Bone changes with osteoarthritis. In: Eskola H, Väisänen O, Viik J, & Hyttinen J (eds) EMBEC & NBC 2017 65. Singapore, Springer Singapore: 900–903. DOI: https://doi.org/10.1007/978-981-10-5122-7_225.

[11] Mishra AK, Kim D & Andayana I (2011) Development of three dimensional binary patterns for local bone structure analysis. In: 2011 IEEE International Conference on Bioinformatics and Biomedicine Workshops (BIBMW): 1006–1008. DOI: https://doi.org/10.1109/BIBMW.2011.6112540.

[12] Otsu N (1979) A threshold selection method from gray-level histograms. IEEE Transactions on Systems, Man, and Cybernetics 9(1): 62–66. DOI: https://doi.org/10.1109/TSMC.1979.4310076.

[13] Modayur B, Prothero J, Ojemann G, Maravilla K & Brinkley J (1997) Visualization-based mapping of language function in the brain. NeuroImage 6(4): 245–258. DOI: https://doi.org/10.1006/nimg.1997.0301.

[14] Caselles V, Kimmel R & Sapiro G (1997) Geodesic active contours. International Journal of Computer Vision 22(1): 61–79. DOI: https://doi.org/10.1023/A:1007979827043.

[15] Uchida S (2013) Image processing and recognition for biological images. Development, Growth & Differentiation 55(4): 523–549. DOI: https://doi.org/10.1111/dgd.12054.

[16] Thevenot J, Chen J, Finnilä M, Nieminen M, Lehenkari P, Saarakkala S & Pietikäinen M (2015) Local binary patterns to evaluate trabecular bone structure from micro-CT data: Application to studies of human osteoarthritis. In: Agapito L, Bronstein MM, & Rother C (eds) Computer Vision - ECCV 2014 Workshops 8926. Cham, Springer International Publishing: 63–79. DOI: https://doi.org/10.1007/978-3-319-16181-5_5.

[17] Zhang Z-M, Li Z-C, Jiang L-S, Jiang S-D & Dai L-Y (2010) Micro-CT and mechanical evaluation of subchondral trabecular bone structure between postmenopausal women with osteoarthritis and osteoporosis. Osteoporosis International 21(8): 1383–1390. DOI: https://doi.org/10.1007/s00198-009-1071-2.

[18] Tabor Z & Latała Z (2014) 3D gray-level histomorphometry of trabecular bone - A methodological review. Image Analysis & Stereology 33(1): 1. DOI: https://doi.org/10.5566/ias.v33.p1-12.

[19] Erlandsson K, Buvat I, Pretorius PH, Thomas BA & Hutton BF (2012) A review of partial volume correction techniques for emission tomography

and their applications in neurology, cardiology and oncology. Physics in Medicine and Biology 57(21): R119–R159. DOI: https://doi.org/10.1088/0031-9155/57/21/R119.

[20] Ojala T, Pietikäinen M & Mäenpää T (2000) Gray scale and rotation invariant texture classification with local binary patterns. In: Computer Vision - ECCV 2000: 6th European Conference on Computer Vision Dublin, Ireland, June 26 – July 1, 2000 Proceedings, Part I. Berlin, Heidelberg, Springer Berlin Heidelberg: 404–420. DOI: https://doi.org/10.1007/3-540-45054-8_27.

[21] Ojala T, Pietikäinen M & Harwood D (1996) A comparative study of texture measures with classification based on featured distributions. Pattern Recognition 29(1): 51–59. DOI: https://doi.org/10.1016/0031-3203(95)00067-4.

[22] Huang D, Shan C, Ardabilian M, Wang Y & Chen L (2011) Local binary patterns and its application to facial image analysis: A survey. IEEE Transactions on Systems, Man, and Cybernetics, Part C (Applications and Reviews) 41(6): 765–781. DOI: https://doi.org/10.1109/TSMCC.2011.2118750.

[23] Bordallo López M, Nieto A, Boutellier J, Hannuksela J & Silvén O (2017) Evaluation of real-time LBP computing in multiple architectures. Journal of Real-Time Image Processing 13(2): 375–396. DOI: https://doi.org/10.1007/s11554-014-0410-5.

[24] Bradley D & Roth G (2007) Adaptive thresholding using the integral image. Journal of Graphics Tools 12(2): 13–21. DOI: https://doi.org/10.1080/2151237X.2007.10129236.

[25] Fisher R, Perkins S, Walker A & Wolfart E (2003) Adaptive thresholding. Hypermedia Image Processing Reference. URL: http://homepages.inf.ed.ac.uk/rbf/HIPR2/adpthrsh.htm. Accessed 09.11.2017.

[26] Boas FE & Fleischmann D (2012) CT artifacts: Causes and reduction techniques. Imaging in Medicine 4(2): 229–240. DOI: https://doi.org/10.2217/iim.12.13.

[27] Goldman LW (2007) Principles of CT and CT technology. Journal of Nuclear Medicine Technology 35(3): 115–128. DOI: https://doi.org/10.2967/jnmt.107.042978.

11. APPENDICES

Appendix 1. Segmented thickness phantom measurements for the 9 µm resolution

Table 8. Tb.Th and percent error for all foils and segmentation parameters

Parameter			Volumetric Tb.Th (µm)				Percent error (%)				
			Foil				Foil				
W	*T*	*C*	20	50	125	250	20	50	125	250	Mean
5	14	17	17.42	39.27	121.05	246.71	12.89	21.45	3.16	1.31	9.70
		18	17.42	35.20	120.27	241.17	12.89	29.61	3.78	3.53	12.45
		19	0.00	34.83	115.24	240.52	100.00	30.35	7.81	3.79	35.49
	15	17	17.42	49.34	121.44	254.18	12.89	1.31	2.85	1.67	4.68
		18	17.42	41.00	121.13	249.42	12.89	18.00	3.09	0.23	8.55
		19	0.00	35.62	120.78	241.89	100.00	28.77	3.38	3.24	33.85
	16	17	17.42	52.05	124.34	256.83	12.89	4.10	0.53	2.73	5.06
		18	17.42	50.31	121.79	255.32	12.89	0.61	2.57	2.13	4.55
		19	0.00	43.08	121.17	251.63	100.00	13.85	3.07	0.65	29.39
	17	17	17.46	52.19	132.82	257.38	12.72	4.38	6.26	2.95	6.58
		18	17.42	52.11	125.84	257.07	12.89	4.23	0.67	2.83	5.16
		19	17.42	51.06	122.47	256.10	12.89	2.13	2.02	2.44	4.87
7	14	17	17.85	51.97	121.13	247.83	10.73	3.94	3.10	0.87	4.66
		18	17.49	50.50	120.89	242.08	12.54	1.01	3.29	3.17	5.00
		19	17.44	45.37	119.65	240.38	12.82	9.26	4.28	3.85	7.55
	15	17	19.03	52.17	121.50	253.32	4.83	4.34	2.80	1.33	3.33
		18	17.69	52.04	121.17	249.79	11.53	4.07	3.07	0.08	4.69
		19	17.47	50.96	121.05	244.60	12.63	1.93	3.16	2.16	4.97
	16	17	21.98	52.20	123.30	256.25	9.90	4.39	1.36	2.50	4.54
		18	18.51	52.17	121.82	254.51	7.45	4.35	2.54	1.80	4.04
		19	17.58	52.08	121.19	251.53	12.10	4.16	3.05	0.61	4.98
	17	17	26.44	52.24	128.34	257.21	32.20	4.48	2.67	2.89	10.56
		18	20.84	52.20	124.22	256.45	4.21	4.40	0.62	2.58	2.95
		19	18.19	52.18	122.20	255.40	9.05	4.36	2.24	2.16	4.45
9	14	17	29.80	52.19	121.16	248.28	48.98	4.39	3.07	0.69	14.28
		18	24.58	52.18	121.06	243.32	22.91	4.37	3.15	2.67	8.28
		19	20.15	52.16	120.61	240.47	0.76	4.32	3.52	3.81	3.10
	15	17	32.50	52.21	121.41	253.11	62.49	4.41	2.87	1.25	17.76
		18	28.32	52.20	121.19	249.81	41.58	4.39	3.05	0.08	12.28
		19	23.18	52.19	121.10	245.15	15.88	4.37	3.12	1.94	6.33
	16	17	33.86	52.24	122.53	255.87	69.32	4.49	1.98	2.35	19.54
		18	31.59	52.21	121.65	253.97	57.97	4.41	2.68	1.59	16.66
		19	26.90	52.20	121.20	251.35	34.52	4.39	3.04	0.54	10.62
	17	17	34.45	52.70	125.63	256.88	72.27	5.40	0.51	2.75	20.23
		18	33.44	52.26	123.18	256.23	67.21	4.51	1.46	2.49	18.92
		19	30.54	52.21	121.93	255.07	52.70	4.41	2.46	2.03	15.40
11	14	17	34.53	52.25	121.18	248.55	72.63	4.50	3.06	0.58	20.19
		18	33.82	52.21	121.10	243.85	69.11	4.42	3.12	2.46	19.78
		19	31.75	52.20	120.91	240.81	58.76	4.41	3.28	3.68	17.53
	15	17	34.66	52.61	121.31	252.57	73.29	5.21	2.95	1.03	20.62

		18	34.39	52.26	121.20	249.59	71.96	4.51	3.04	0.16	19.92
		19	33.36	52.21	121.14	245.50	66.80	4.42	3.09	1.80	19.03
	16	17	34.71	53.88	122.21	255.23	73.55	7.75	2.23	2.09	21.41
		18	34.62	52.62	121.54	253.52	73.08	5.24	2.76	1.41	20.62
		19	34.19	52.28	121.25	251.09	70.93	4.55	3.00	0.44	19.73
	17	17	34.72	56.84	124.32	256.60	73.62	13.68	0.54	2.64	22.62
		18	34.67	53.94	122.54	255.75	73.34	7.87	1.97	2.30	21.37
		19	34.55	52.63	121.69	254.36	72.74	5.26	2.65	1.74	20.60

Table 9. Tb.Th of 20 µm foil segmented with different values of *W*, *T, C* (µm)

C[6]	*W*	*T*			
		14	15	16	17
17	5	17.42114	17.42114	17.42114	17.457
	7	17.85487	19.03467	21.98004	26.44034
	9	29.79557	32.49897	33.86425	34.45438
	11	34.52608	34.65884	34.70929	34.7236
18	5	17.42114	17.42114	17.42114	17.42114
	7	17.49184	17.69393	18.50962	20.84186
	9	24.5811	28.31598	31.59447	33.44189
	11	33.82291	34.39135	34.61504	34.66871
19	5	0	0	0	17.42114
	7	17.43518	17.47462	17.58065	18.19097
	9	20.15177	23.17509	26.90368	30.54046
	11	31.75168	33.35993	34.18646	34.54797

[6] Normalized to integer range 0-255

Table 10. Tb.Th of 50 μm foil segmented with different values of *W, T, C* (μm)

C	*W*	*T*			
		14	15	16	17
17	5	39.27318	49.34460	52.04919	52.18870
	7	51.96777	52.17197	52.19503	52.23777
	9	52.19417	52.20510	52.24366	52.70147
	11	52.24808	52.60695	53.87582	56.83908
18	5	35.19732	41.00089	50.30652	52.11256
	7	50.50277	52.03735	52.17427	52.19760
	9	52.18305	52.19548	52.20646	52.25511
	11	52.20982	52.25585	52.62078	53.93521
19	5	34.82747	35.61677	43.07648	51.06277
	7	45.36820	50.96417	52.08238	52.17935
	9	52.15802	52.18648	52.19717	52.20691
	11	52.20274	52.20993	52.27730	52.63241

Table 11. Tb.Th of 125 μm foil segmented with different values of *W, T, C* (μm)

C	*W*	*T*			
		14	15	16	17
17	5	121.05474	121.43589	124.34008	132.81965
	7	121.12678	121.49825	123.29595	128.34271
	9	121.15928	121.40947	122.52592	125.63163
	11	121.17701	121.30839	122.20763	124.32447
18	5	120.27483	121.13240	121.79060	125.83740
	7	120.88697	121.16737	121.82359	124.22490
	9	121.05805	121.18616	121.65136	123.17674
	11	121.09527	121.20110	121.54443	122.53677
19	5	115.24303	120.78007	121.16634	122.47115
	7	119.65170	121.04711	121.18791	122.19777
	9	120.60562	121.10352	121.20406	121.92973
	11	120.90585	121.14057	121.24666	121.69323

Table 12. Tb.Th of 250 μm foil segmented with different values of *W, T, C* (μm).

C	*W*	*T*			
		14	15	16	17
17	5	246.71355	254.17534	256.82845	257.38278
	7	247.83027	253.32201	256.25493	257.21331
	9	248.27827	253.11380	255.86906	256.87551
	11	248.55072	252.57162	255.22682	256.60354
18	5	241.16777	249.41774	255.32078	257.06661
	7	242.08291	249.79400	254.50840	256.45301
	9	243.32450	249.80732	253.96501	256.22682
	11	243.84553	249.58902	253.52210	255.75472
19	5	240.52281	241.88899	251.63212	256.10204
	7	240.38183	244.60025	251.52674	255.39922
	9	240.46502	245.14903	251.35153	255.07407
	11	240.80748	245.50359	251.09042	254.36148

Appendix 2. Segmented thickness phantom measurements for the 18 µm resolution

Table 13. Tb.Th of foils segmented with different values of *W, T, C* (µm)

Parameter			Volumetric Tb.Th (µm)			Percent error (%)				
W	*T*	*C*	Foil			Foil				
			50	125	250	50	125	250	Mean[7]	Mean[8]
3	50	47	34.84	138.13	248.40	30.32	10.50	0.64	13.82	5.57
5	10	10	69.53	124.27	241.36	39.07	0.59	3.46	14.37	2.02
5	14	17	62.18	104.95	241.15	24.36	16.04	3.54	14.65	9.79
5	17	18	68.48	116.35	241.39	36.96	6.92	3.44	15.77	5.18
5	18	18	69.22	124.88	241.44	38.44	0.10	3.42	13.99	1.76
5	18	22	39.52	104.51	241.19	20.96	16.39	3.52	13.62	9.96
5	22	22	67.37	124.99	241.45	34.74	0.01	3.42	12.72	1.72
5	30	29	59.24	131.58	241.49	18.48	5.26	3.40	9.05	4.33
5	30	30	48.11	125.36	241.46	3.78	0.29	3.42	2.49	1.85
5	31	29	65.41	136.14	242.75	30.81	8.91	2.90	14.21	5.91
5	31	30	56.70	131.50	241.50	13.39	5.20	3.40	7.33	4.30
5	38	33	68.77	138.51	257.25	37.53	10.81	2.90	17.08	6.85
5	38	34	69.44	138.22	245.93	38.89	10.57	1.63	17.03	6.10
5	39	32	69.42	138.69	264.12	38.84	10.95	5.65	18.48	8.30
5	39	35	64.53	138.33	250.71	29.06	10.66	0.28	13.34	5.47
5	39	38	37.62	131.46	241.53	24.76	5.17	3.39	11.11	4.28
5	39	39	35.35	125.32	241.55	29.30	0.26	3.38	10.98	1.82
5	40	34	69.17	138.54	260.91	38.33	10.83	4.36	17.84	7.60
5	40	37	52.30	137.92	244.68	4.60	10.33	2.13	5.69	6.23
5	40	40	35.21	125.33	241.49	29.58	0.27	3.40	11.08	1.84
5	50	29	69.63	167.16	277.82	39.26	33.73	11.13	28.04	22.43
5	50	47	35.57	137.76	255.51	28.86	10.21	2.21	13.76	6.21
5	100	85	50.73	138.15	257.69	1.45	10.52	3.07	5.01	6.80
5	100	88	39.32	136.67	257.29	21.37	9.33	2.92	11.21	6.13
5	100	92	34.88	125.77	257.27	30.25	0.61	2.91	11.26	1.76
7	17	18	69.55	120.37	241.40	39.09	3.71	3.44	15.41	3.57
7	30	29	69.43	131.57	241.48	38.86	5.26	3.41	15.84	4.33
7	31	31	69.25	126.95	241.36	38.50	1.56	3.46	14.51	2.51
7	38	32	69.54	138.54	257.19	39.07	10.83	2.88	17.59	6.85
7	38	33	69.49	138.46	252.20	38.98	10.76	0.88	16.88	5.82
7	50	47	57.74	137.46	242.76	15.48	9.97	2.89	9.45	6.43

[7] Foils: 50 µm, 125 µm, 250 µm
[8] Foils: 125 µm, 250 µm

Appendix 3. Segmented thickness phantom measurements for the 35 µm resolution

Table 14. Tb.Th of foils segmented with different values of *W, T, C* (µm)

Parameter			Volumetric Tb.Th (µm)		Relative error (%)		
W	*T*	*C*	Foil		Foil		
			125	250	125	250	Mean
3	14	26	116.85	208.15	6.52	16.74	11.63
3	14	28	82.85	208.18	33.72	16.73	25.22
3	15	25	135.04	214.22	8.03	14.31	11.17
3	17	17	139.22	275.08	11.38	10.03	10.70
3	17	25	137.88	260.03	10.31	4.01	7.16
3	17	26	138.26	241.87	10.61	3.25	6.93
3	17	29	131.45	210.45	5.16	15.82	10.49
3	30	30	139.24	276.14	11.39	10.46	10.93
3	30	45	137.68	242.99	10.15	2.80	6.48
3	40	45	139.22	275.79	11.38	10.32	10.85
3	40	60	137.00	238.64	9.60	4.54	7.07
3	40	65	106.98	208.39	14.42	16.64	15.53
3	40	70	70.42	208.30	43.66	16.68	30.17
3	40	80	69.68	207.33	44.25	17.07	30.66
3	45	70	128.21	211.44	2.57	15.42	9.00
3	50	70	138.65	271.22	10.92	8.49	9.70
3	50	75	135.54	234.81	8.44	6.08	7.26
3	50	80	103.37	208.43	17.30	16.63	16.96
3	54	60	138.98	276.10	11.18	10.44	10.81
3	100	127	138.82	275.67	11.05	10.27	10.66
5	17	17	138.80	274.62	11.04	9.85	10.44
5	17	19	139.21	274.46	11.37	9.78	10.58
5	32	40	139.18	274.52	11.34	9.81	10.58
13	14	24	134.64	211.15	7.71	15.54	11.62
27	17	50	139.16	275.75	11.33	10.30	10.81
27	17	64	138.00	263.54	10.40	5.42	7.91

Appendix 4. Effect of different neighborhood parameters on segmentation time and on similarity to GT at 9 µm resolution

Table 15. Effect of different neighborhood parameters on segmentation time and similarity to the GT, fixed cubical 6.7 mm (256 x 256 x 256) VOI in 9 µm scan of bovine trabecular bone sample 1

Neighborhood parameter				MSE	SSIM	Segmentation time (s)
R_1 (px)	N_1	R_2 (px)	N_2			
0.692	18	1.69	54	2245.7986	0.1689	189
0.692	18	1.69	78	2245.8093	0.1689	183
0.692	18	1.69	114	2245.9201	0.1688	183
0.692	18	2	54	2245.7976	0.1689	183
0.692	18	2	78	2245.7998	0.1689	180
0.692	18	2	114	2245.8363	0.1689	181
0.692	18	2.46	54	2245.7949	0.1689	184
0.692	18	2.46	78	2245.8068	0.1689	184
0.692	18	2.46	114	2245.8098	0.1689	184
0.692	26	1.69	54	2245.7949	0.1689	189
0.692	26	1.69	78	2245.7949	0.1689	189
0.692	26	1.69	114	2245.7949	0.1689	190
0.692	26	2	54	2245.7949	0.1689	192
0.692	26	2	78	2245.7949	0.1689	190
0.692	26	2	114	2245.7949	0.1689	189
0.692	26	2.46	54	2245.7949	0.1689	191
0.692	26	2.46	78	2245.7949	0.1689	191
0.692	26	2.46	114	2245.7949	0.1689	192
0.692	38	1.69	54	2245.7949	0.1689	201
0.692	38	1.69	78	2245.7949	0.1689	202
0.692	38	1.69	114	2245.7949	0.1689	203
0.692	38	2	54	2245.7949	0.1689	200
0.692	38	2	78	2245.7949	0.1689	199
0.692	38	2	114	2245.7949	0.1689	198
0.692	38	2.46	54	2245.7949	0.1689	205
0.692	38	2.46	78	2245.7949	0.1689	203
0.692	38	2.46	114	2245.7949	0.1689	203
1	18	1.69	54	2150.9040	0.1770	189
1	18	1.69	78	2154.7906	0.1766	189
1	18	1.69	114	2149.8950	0.1771	184
1	18	2	54	2147.2359	0.1773	185
1	18	2	78	2152.4855	0.1768	185
1	18	2	114	2150.2976	0.1770	184
1	18	2.46	54	2152.4847	0.1768	187
1	18	2.46	78	2156.9338	0.1764	187
1	18	2.46	114	2149.9053	0.1771	188
1	26	1.69	54	2137.0102	0.1783	197
1	26	1.69	78	2138.1399	0.1781	192
1	26	1.69	114	2138.9928	0.1781	193

1	26	2	54	2139.4689	0.1780	192
1	26	2	78	2137.3513	0.1782	193
1	26	2	114	2141.5018	0.1778	193
1	26	2.46	54	2135.6574	0.1784	204
1	26	2.46	78	2135.1519	0.1784	194
1	26	2.46	114	2145.9684	0.1774	194
1	38	1.69	54	2131.3817	0.1788	203
1	38	1.69	78	2129.2150	0.1790	204
1	38	1.69	114	2126.9313	0.1792	213
1	38	2	54	2126.6385	0.1792	211
1	38	2	78	2126.9034	0.1792	205
1	38	2	114	2125.9435	0.1793	212
1	38	2.46	54	2124.1361	0.1795	209
1	38	2.46	78	2125.9438	0.1793	207
1	38	2.46	114	2128.0567	0.1791	208
1.46	18	1.69	54	1987.3756	0.1932	448
1.46	18	1.69	78	1979.3045	0.1941	310
1.46	18	1.69	114	1981.2285	0.1939	310
1.46	18	2	54	1977.3584	0.1943	308
1.46	18	2	78	1987.5815	0.1932	306
1.46	18	2	114	1985.4729	0.1934	306
1.46	18	2.46	54	1985.5360	0.1934	321
1.46	18	2.46	78	1988.9079	0.1931	320
1.46	18	2.46	114	1985.4732	0.1934	319
1.46	26	1.69	54	1967.1020	0.1954	372
1.46	26	1.69	78	1962.8346	0.1959	370
1.46	26	1.69	114	1969.1435	0.1952	372
1.46	26	2	54	1963.9886	0.1958	359
1.46	26	2	78	1969.4611	0.1951	356
1.46	26	2	114	1967.8634	0.1953	358
1.46	26	2.46	54	1968.9943	0.1952	370
1.46	26	2.46	78	1971.2314	0.1950	369
1.46	26	2.46	114	1970.4606	0.1950	374
1.46	38	1.69	54	1956.9966	0.1965	442
1.46	38	1.69	78	1959.8632	0.1962	445
1.46	38	1.69	114	1961.7200	0.1960	440
1.46	38	2	54	1961.2966	0.1960	416
1.46	38	2	78	1957.2300	0.1965	411
1.46	38	2	114	1961.1955	0.1960	412
1.46	38	2.46	54	1962.4289	0.1959	435
1.46	38	2.46	78	1958.0720	0.1964	443
1.46	38	2.46	114	1961.4991	0.1960	443

Table 16. Effect of different neighborhood parameters on segmentation time and similarity to the GT, fixed cubical 6.7 mm (256 x 256 x 256) VOI in 9 µm scan of bovine trabecular bone sample 2

Neighborhood parameter				MSE	SSIM	Segmentation time (s)
R_1 (px)	N_1	R_2 (px)	N_2			
0.692	18	1.69	54	1619.2043	0.1147	311
0.692	18	1.69	78	1619.4123	0.1147	175
0.692	18	1.69	114	1619.4015	0.1147	177
0.692	18	2	54	1619.2059	0.1147	176
0.692	18	2	78	1619.2535	0.1147	176
0.692	18	2	114	1619.2732	0.1147	176
0.692	18	2.46	54	1619.2043	0.1147	178
0.692	18	2.46	78	1619.2085	0.1147	179
0.692	18	2.46	114	1619.2142	0.1147	179
0.692	26	1.69	54	1619.2043	0.1147	185
0.692	26	1.69	78	1619.2043	0.1147	184
0.692	26	1.69	114	1619.2043	0.1147	185
0.692	26	2	54	1619.2043	0.1147	185
0.692	26	2	78	1619.2043	0.1147	185
0.692	26	2	114	1619.2043	0.1147	188
0.692	26	2.46	54	1619.2043	0.1147	186
0.692	26	2.46	78	1619.2043	0.1147	187
0.692	26	2.46	114	1619.2043	0.1147	186
0.692	38	1.69	54	1619.2043	0.1147	201
0.692	38	1.69	78	1619.2043	0.1147	196
0.692	38	1.69	114	1619.2043	0.1147	196
0.692	38	2	54	1619.2043	0.1147	197
0.692	38	2	78	1619.2043	0.1147	196
0.692	38	2	114	1619.2043	0.1147	196
0.692	38	2.46	54	1619.2043	0.1147	198
0.692	38	2.46	78	1619.2043	0.1147	198
0.692	38	2.46	114	1619.2043	0.1147	198
1	18	1.69	54	1544.9649	0.1208	184
1	18	1.69	78	1540.1560	0.1212	180
1	18	1.69	114	1544.9718	0.1207	178
1	18	2	54	1543.4439	0.1208	177
1	18	2	78	1540.1533	0.1212	183
1	18	2	114	1540.1545	0.1212	182
1	18	2.46	54	1545.0134	0.1208	181
1	18	2.46	78	1543.4562	0.1208	181
1	18	2.46	114	1545.0112	0.1208	181
1	26	1.69	54	1533.6902	0.1218	186
1	26	1.69	78	1529.3158	0.1221	192
1	26	1.69	114	1533.6712	0.1218	189
1	26	2	54	1533.9011	0.1217	186
1	26	2	78	1536.0256	0.1215	187
1	26	2	114	1532.4372	0.1219	185

1	26	2.46	54	1531.9113	0.1219	189
1	26	2.46	78	1535.7054	0.1215	189
1	26	2.46	114	1539.2971	0.1213	188
1	38	1.69	54	1525.8423	0.1224	197
1	38	1.69	78	1523.9764	0.1226	198
1	38	1.69	114	1528.5673	0.1222	197
1	38	2	54	1526.3611	0.1224	200
1	38	2	78	1528.2949	0.1222	198
1	38	2	114	1526.6798	0.1224	202
1	38	2.46	54	1525.8312	0.1224	200
1	38	2.46	78	1528.1270	0.1222	200
1	38	2.46	114	1526.3450	0.1224	200
1.46	18	1.69	54	1430.6925	0.1316	413
1.46	18	1.69	78	1426.2402	0.1321	297
1.46	18	1.69	114	1426.1060	0.1321	299
1.46	18	2	54	1430.8071	0.1316	297
1.46	18	2	78	1426.1979	0.1321	298
1.46	18	2	114	1424.4407	0.1322	316
1.46	18	2.46	54	1430.5313	0.1317	305
1.46	18	2.46	78	1430.8341	0.1316	308
1.46	18	2.46	114	1426.5838	0.1320	306
1.46	26	1.69	54	1414.7779	0.1333	360
1.46	26	1.69	78	1416.7222	0.1331	360
1.46	26	1.69	114	1419.1071	0.1328	362
1.46	26	2	54	1415.7799	0.1332	343
1.46	26	2	78	1418.4078	0.1329	344
1.46	26	2	114	1416.1551	0.1332	347
1.46	26	2.46	54	1417.8027	0.1330	353
1.46	26	2.46	78	1414.9937	0.1333	355
1.46	26	2.46	114	1415.6210	0.1332	354
1.46	38	1.69	54	1411.1106	0.1337	427
1.46	38	1.69	78	1410.2555	0.1338	423
1.46	38	1.69	114	1412.3720	0.1335	427
1.46	38	2	54	1412.3459	0.1336	401
1.46	38	2	78	1412.4809	0.1335	402
1.46	38	2	114	1411.1403	0.1337	403
1.46	38	2.46	54	1411.5248	0.1336	423
1.46	38	2.46	78	1413.1094	0.1335	443
1.46	38	2.46	114	1411.1251	0.1337	417

Appendix 5. Effect of different neighborhood parameters on segmentation time and on similarity to GT at 18 µm resolution

Table 17. Effect of different neighborhood parameters on segmentation time and similarity to the GT, fixed cubical 6.7 mm (128 x 128 x 128) VOI in 18 µm scan of bovine trabecular bone sample 1

Neighborhood parameter				MSE	SSIM	Segmentation time (s)
R_1 (px)	N_1	R_2 (px)	N_2			
0.692	18	1.69	54	2046.0355	0.2715	55
0.692	18	1.69	78	2046.4170	0.2714	23
0.692	18	1.69	114	2046.2209	0.2714	22
0.692	18	2	54	2046.0391	0.2715	22
0.692	18	2	78	2046.1356	0.2715	23
0.692	18	2	114	2046.1332	0.2715	23
0.692	18	2.46	54	2046.0315	0.2715	24
0.692	18	2.46	78	2046.0315	0.2715	24
0.692	18	2.46	114	2046.0705	0.2715	23
0.692	26	1.69	54	2046.0315	0.2715	23
0.692	26	1.69	78	2046.0315	0.2715	24
0.692	26	1.69	114	2046.0315	0.2715	24
0.692	26	2	54	2046.0315	0.2715	24
0.692	26	2	78	2046.0315	0.2715	24
0.692	26	2	114	2046.0315	0.2715	25
0.692	26	2.46	54	2046.0315	0.2715	25
0.692	26	2.46	78	2046.0315	0.2715	25
0.692	26	2.46	114	2046.0315	0.2715	25
0.692	38	1.69	54	2046.0315	0.2715	26
0.692	38	1.69	78	2046.0315	0.2715	26
0.692	38	1.69	114	2046.0315	0.2715	26
0.692	38	2	54	2046.0315	0.2715	26
0.692	38	2	78	2046.0315	0.2715	26
0.692	38	2	114	2046.0315	0.2715	26
0.692	38	2.46	54	2046.0315	0.2715	27
0.692	38	2.46	78	2046.0315	0.2715	27
0.692	38	2.46	114	2046.0315	0.2715	27
1	18	1.69	54	1894.0138	0.2876	24
1	18	1.69	78	1895.8107	0.2875	24
1	18	1.69	114	1894.0087	0.2876	23
1	18	2	54	1901.3047	0.2868	23
1	18	2	78	1895.8189	0.2875	26
1	18	2	114	1895.8184	0.2875	24
1	18	2.46	54	1899.0472	0.2870	25
1	18	2.46	78	1901.3454	0.2868	25
1	18	2.46	114	1899.0559	0.2870	24
1	26	1.69	54	1882.0199	0.2888	24
1	26	1.69	78	1871.3462	0.2900	25
1	26	1.69	114	1881.8658	0.2888	26

1	26	2	54	1880.4774	0.2891	25
1	26	2	78	1872.8763	0.2899	26
1	26	2	114	1881.5511	0.2890	25
1	26	2.46	54	1877.8261	0.2893	26
1	26	2.46	78	1879.4154	0.2892	26
1	26	2.46	114	1882.3694	0.2888	25
1	38	1.69	54	1860.6935	0.2912	27
1	38	1.69	78	1854.0457	0.2920	27
1	38	1.69	114	1857.3186	0.2916	27
1	38	2	54	1854.8909	0.2919	28
1	38	2	78	1858.7975	0.2915	27
1	38	2	114	1858.4099	0.2914	29
1	38	2.46	54	1860.6977	0.2912	29
1	38	2.46	78	1865.5522	0.2907	28
1	38	2.46	114	1856.7734	0.2917	28
1.46	18	1.69	54	1652.7136	0.3153	65
1.46	18	1.69	78	1641.2912	0.3166	55
1.46	18	1.69	114	1644.2762	0.3163	55
1.46	18	2	54	1653.8426	0.3152	55
1.46	18	2	78	1641.0115	0.3166	55
1.46	18	2	114	1638.5503	0.3168	55
1.46	18	2.46	54	1655.0820	0.3149	55
1.46	18	2.46	78	1653.8607	0.3152	55
1.46	18	2.46	114	1641.0420	0.3165	55
1.46	26	1.69	54	1624.4358	0.3186	56
1.46	26	1.69	78	1618.4543	0.3193	56
1.46	26	1.69	114	1627.3816	0.3183	56
1.46	26	2	54	1623.3695	0.3187	55
1.46	26	2	78	1626.0585	0.3185	55
1.46	26	2	114	1626.4910	0.3185	55
1.46	26	2.46	54	1627.0321	0.3183	56
1.46	26	2.46	78	1621.5690	0.3190	57
1.46	26	2.46	114	1621.1228	0.3190	57
1.46	38	1.69	54	1610.6526	0.3202	64
1.46	38	1.69	78	1614.4923	0.3198	64
1.46	38	1.69	114	1616.9991	0.3195	64
1.46	38	2	54	1616.9593	0.3195	61
1.46	38	2	78	1613.6777	0.3199	61
1.46	38	2	114	1612.9043	0.3200	61
1.46	38	2.46	54	1601.9238	0.3211	69
1.46	38	2.46	78	1614.1489	0.3198	68
1.46	38	2.46	114	1613.7105	0.3199	65

Table 18. Effect of different neighborhood parameters on segmentation time and similarity to the GT, fixed cubical 6.7 mm (128 x 128 x 128) VOI in 18 µm scan of bovine trabecular bone sample 2

Neighborhood parameter				MSE	SSIM	Segmentation time (s)
R_1 (px)	N_1	R_2 (px)	N_2			
0.692	18	1.69	54	1370.2942	0.1950	55
0.692	18	1.69	78	1370.6182	0.1949	21
0.692	18	1.69	114	1370.6228	0.1949	21
0.692	18	2	54	1370.2904	0.1950	21
0.692	18	2	78	1370.3734	0.1950	21
0.692	18	2	114	1370.4179	0.1950	21
0.692	18	2.46	54	1370.2901	0.1950	21
0.692	18	2.46	78	1370.3019	0.1950	22
0.692	18	2.46	114	1370.3508	0.1950	22
0.692	26	1.69	54	1370.2864	0.1950	22
0.692	26	1.69	78	1370.2864	0.1950	22
0.692	26	1.69	114	1370.2864	0.1950	22
0.692	26	2	54	1370.2864	0.1950	22
0.692	26	2	78	1370.2864	0.1950	23
0.692	26	2	114	1370.2864	0.1950	23
0.692	26	2.46	54	1370.2864	0.1950	23
0.692	26	2.46	78	1370.2864	0.1950	23
0.692	26	2.46	114	1370.2864	0.1950	23
0.692	38	1.69	54	1370.2864	0.1950	24
0.692	38	1.69	78	1370.2864	0.1950	24
0.692	38	1.69	114	1370.2864	0.1950	25
0.692	38	2	54	1370.2864	0.1950	24
0.692	38	2	78	1370.2864	0.1950	24
0.692	38	2	114	1370.2864	0.1950	24
0.692	38	2.46	54	1370.2864	0.1950	25
0.692	38	2.46	78	1370.2864	0.1950	25
0.692	38	2.46	114	1370.2864	0.1950	25
1	18	1.69	54	1256.5706	0.2081	22
1	18	1.69	78	1248.6254	0.2091	22
1	18	1.69	114	1256.5495	0.2081	22
1	18	2	54	1253.6605	0.2085	21
1	18	2	78	1248.6019	0.2091	23
1	18	2	114	1248.6118	0.2091	23
1	18	2.46	54	1256.4176	0.2081	22
1	18	2.46	78	1253.7046	0.2085	23
1	18	2.46	114	1256.4204	0.2081	22
1	26	1.69	54	1239.7922	0.2102	23
1	26	1.69	78	1232.6480	0.2111	24
1	26	1.69	114	1239.7829	0.2102	24
1	26	2	54	1239.7901	0.2103	23
1	26	2	78	1243.3559	0.2098	23
1	26	2	114	1237.5891	0.2105	23

1	26	2.46	54	1236.9084	0.2106	24
1	26	2.46	78	1242.8066	0.2099	24
1	26	2.46	114	1248.2139	0.2092	23
1	38	1.69	54	1228.1284	0.2117	25
1	38	1.69	78	1225.2803	0.2121	25
1	38	1.69	114	1232.6120	0.2112	25
1	38	2	54	1229.4479	0.2115	25
1	38	2	78	1231.8085	0.2113	25
1	38	2	114	1229.8798	0.2115	27
1	38	2.46	54	1228.1184	0.2117	25
1	38	2.46	78	1231.9190	0.2113	26
1	38	2.46	114	1229.7012	0.2115	27
1.46	18	1.69	54	1101.5913	0.2294	60
1.46	18	1.69	78	1096.2030	0.2303	55
1.46	18	1.69	114	1096.0232	0.2303	55
1.46	18	2	54	1102.1300	0.2294	55
1.46	18	2	78	1096.1468	0.2303	55
1.46	18	2	114	1093.8726	0.2306	55
1.46	18	2.46	54	1101.1708	0.2295	55
1.46	18	2.46	78	1102.1421	0.2294	55
1.46	18	2.46	114	1096.4434	0.2302	55
1.46	26	1.69	54	1082.0972	0.2324	55
1.46	26	1.69	78	1084.5269	0.2320	55
1.46	26	1.69	114	1087.2803	0.2316	55
1.46	26	2	54	1083.2687	0.2322	55
1.46	26	2	78	1086.5066	0.2318	55
1.46	26	2	114	1083.7615	0.2321	55
1.46	26	2.46	54	1085.3448	0.2319	55
1.46	26	2.46	78	1081.6481	0.2324	55
1.46	26	2.46	114	1082.8093	0.2323	55
1.46	38	1.69	54	1077.4331	0.2332	62
1.46	38	1.69	78	1076.0931	0.2333	61
1.46	38	1.69	114	1078.7899	0.2329	61
1.46	38	2	54	1078.7840	0.2329	58
1.46	38	2	78	1078.9479	0.2329	59
1.46	38	2	114	1077.5824	0.2331	59
1.46	38	2.46	54	1077.7152	0.2331	63
1.46	38	2.46	78	1079.8916	0.2328	65
1.46	38	2.46	114	1077.3351	0.2332	61

Appendix 6. Effect of different neighborhood parameters on segmentation time and on similarity to GT at 35 µm resolution

Table 19. Effect of different neighborhood parameters on segmentation time and similarity to the GT, fixed cubical 6.7 mm (64 x 64 x 64) VOI in 35 µm scan of bovine trabecular bone sample 1

Neighborhood parameter				MSE	SSIM	Segmentation time (s)
R_1 (px)	N_1	R_2 (px)	N_2			
0.692	18	1.69	54	2307.9211	0.4295	5
0.692	18	1.69	78	2308.3329	0.4294	4
0.692	18	1.69	114	2308.2542	0.4294	3
0.692	18	2	54	2307.8920	0.4295	4
0.692	18	2	78	2308.1062	0.4295	4
0.692	18	2	114	2308.1675	0.4295	3
0.692	18	2.46	54	2307.9590	0.4295	4
0.692	18	2.46	78	2307.8920	0.4295	4
0.692	18	2.46	114	2308.1631	0.4295	4
0.692	26	1.69	54	2307.8621	0.4295	4
0.692	26	1.69	78	2307.8621	0.4295	4
0.692	26	1.69	114	2307.8621	0.4295	4
0.692	26	2	54	2307.8621	0.4295	4
0.692	26	2	78	2307.8621	0.4295	4
0.692	26	2	114	2307.8621	0.4295	4
0.692	26	2.46	54	2307.8621	0.4295	4
0.692	26	2.46	78	2307.8621	0.4295	4
0.692	26	2.46	114	2307.8621	0.4295	4
0.692	38	1.69	54	2307.8621	0.4295	4
0.692	38	1.69	78	2307.8621	0.4295	4
0.692	38	1.69	114	2307.8621	0.4295	4
0.692	38	2	54	2307.8621	0.4295	4
0.692	38	2	78	2307.8621	0.4295	4
0.692	38	2	114	2307.8621	0.4295	4
0.692	38	2.46	54	2307.8621	0.4295	4
0.692	38	2.46	78	2307.8621	0.4295	4
0.692	38	2.46	114	2307.8621	0.4295	4
1	18	1.69	54	2057.7694	0.4523	4
1	18	1.69	78	2061.5419	0.4522	4
1	18	1.69	114	2057.7959	0.4523	4
1	18	2	54	2068.2205	0.4511	4
1	18	2	78	2061.5419	0.4522	4
1	18	2	114	2061.5419	0.4522	4
1	18	2.46	54	2067.0336	0.4514	4
1	18	2.46	78	2068.3293	0.4511	4
1	18	2.46	114	2067.0095	0.4514	4
1	26	1.69	54	2036.9610	0.4540	4
1	26	1.69	78	2020.1875	0.4554	4

1	26	1.69	114	2037.0843	0.4540	4
1	26	2	54	2038.5902	0.4543	4
1	26	2	78	2023.7654	0.4551	4
1	26	2	114	2037.4402	0.4541	4
1	26	2.46	54	2028.1766	0.4548	4
1	26	2.46	78	2035.0326	0.4544	4
1	26	2.46	114	2037.6599	0.4538	4
1	38	1.69	54	2003.4144	0.4572	4
1	38	1.69	78	1992.8589	0.4581	4
1	38	1.69	114	1999.5319	0.4574	4
1	38	2	54	1994.1911	0.4580	4
1	38	2	78	2001.5789	0.4572	4
1	38	2	114	1999.8458	0.4572	4
1	38	2.46	54	2003.4144	0.4572	4
1	38	2.46	78	2009.9996	0.4564	4
1	38	2.46	114	1998.3842	0.4576	5
1.46	18	1.69	54	1691.3226	0.4875	7
1.46	18	1.69	78	1674.0872	0.4892	6
1.46	18	1.69	114	1680.1205	0.4886	6
1.46	18	2	54	1692.8496	0.4875	5
1.46	18	2	78	1673.8144	0.4893	6
1.46	18	2	114	1668.7564	0.4892	6
1.46	18	2.46	54	1693.9476	0.4870	6
1.46	18	2.46	78	1692.8068	0.4875	6
1.46	18	2.46	114	1672.1410	0.4890	6
1.46	26	1.69	54	1647.1383	0.4916	6
1.46	26	1.69	78	1636.7067	0.4924	6
1.46	26	1.69	114	1651.3794	0.4912	7
1.46	26	2	54	1643.0788	0.4919	6
1.46	26	2	78	1652.6116	0.4913	6
1.46	26	2	114	1648.9700	0.4914	6
1.46	26	2.46	54	1652.0169	0.4912	7
1.46	26	2.46	78	1642.0402	0.4919	7
1.46	26	2.46	114	1641.9744	0.4919	7
1.46	38	1.69	54	1624.7432	0.4934	8
1.46	38	1.69	78	1632.4303	0.4928	7
1.46	38	1.69	114	1636.2045	0.4926	7
1.46	38	2	54	1636.2929	0.4926	7
1.46	38	2	78	1631.4503	0.4930	7
1.46	38	2	114	1629.8086	0.4930	7
1.46	38	2.46	54	1612.8309	0.4944	9
1.46	38	2.46	78	1631.3082	0.4929	8
1.46	38	2.46	114	1630.9776	0.4929	8

Table 20. Effect of different neighborhood parameters on segmentation time and similarity to the GT, fixed cubical 6.7 mm (64 x 64 x 64) VOI in 35 μm scan of bovine trabecular bone sample 2

Neighborhood parameter				MSE	SSIM	Segmentation time (s)
R_1 (px)	N_1	R_2 (px)	N_2			
0.692	18	1.69	54	1516.1176	0.3208	5
0.692	18	1.69	78	1516.5564	0.3207	3
0.692	18	1.69	114	1516.7189	0.3207	3
0.692	18	2	54	1516.1650	0.3208	3
0.692	18	2	78	1516.1606	0.3208	3
0.692	18	2	114	1516.1876	0.3208	3
0.692	18	2.46	54	1516.1723	0.3208	3
0.692	18	2.46	78	1516.1759	0.3208	3
0.692	18	2.46	114	1516.3931	0.3208	3
0.692	26	1.69	54	1516.0527	0.3208	3
0.692	26	1.69	78	1516.0527	0.3208	3
0.692	26	1.69	114	1516.0527	0.3208	3
0.692	26	2	54	1516.0527	0.3208	3
0.692	26	2	78	1516.0527	0.3208	3
0.692	26	2	114	1516.0527	0.3208	4
0.692	26	2.46	54	1516.0527	0.3208	4
0.692	26	2.46	78	1516.0527	0.3208	4
0.692	26	2.46	114	1516.0527	0.3208	4
0.692	38	1.69	54	1516.0527	0.3208	4
0.692	38	1.69	78	1516.0527	0.3208	4
0.692	38	1.69	114	1516.0527	0.3208	4
0.692	38	2	54	1516.0527	0.3208	4
0.692	38	2	78	1516.0527	0.3208	4
0.692	38	2	114	1516.0527	0.3208	4
0.692	38	2.46	54	1516.0527	0.3208	4
0.692	38	2.46	78	1516.0527	0.3208	4
0.692	38	2.46	114	1516.0527	0.3208	4
1	18	1.69	54	1342.3682	0.3409	3
1	18	1.69	78	1330.8053	0.3424	4
1	18	1.69	114	1342.3442	0.3409	3
1	18	2	54	1337.1938	0.3415	3
1	18	2	78	1330.8220	0.3424	4
1	18	2	114	1330.7783	0.3424	3
1	18	2.46	54	1343.0195	0.3406	4
1	18	2.46	78	1337.3569	0.3415	4
1	18	2.46	114	1343.0013	0.3406	4
1	26	1.69	54	1315.9277	0.3439	4
1	26	1.69	78	1306.3121	0.3452	4
1	26	1.69	114	1316.0454	0.3439	4

1	26	2	54	1316.0790	0.3443	4
1	26	2	78	1319.6967	0.3437	3
1	26	2	114	1312.5200	0.3445	3
1	26	2.46	54	1311.2590	0.3446	4
1	26	2.46	78	1319.1407	0.3438	4
1	26	2.46	114	1328.2486	0.3427	4
1	38	1.69	54	1299.6164	0.3462	4
1	38	1.69	78	1295.3121	0.3465	4
1	38	1.69	114	1305.7182	0.3455	4
1	38	2	54	1301.3270	0.3459	4
1	38	2	78	1303.9648	0.3456	4
1	38	2	114	1300.7691	0.3459	4
1	38	2.46	54	1299.6164	0.3462	4
1	38	2.46	78	1304.3693	0.3457	4
1	38	2.46	114	1300.4051	0.3460	4
1.46	18	1.69	54	1125.5650	0.3696	7
1.46	18	1.69	78	1118.4032	0.3710	5
1.46	18	1.69	114	1118.1140	0.3710	5
1.46	18	2	54	1125.2866	0.3697	5
1.46	18	2	78	1118.2943	0.3710	5
1.46	18	2	114	1115.3532	0.3711	5
1.46	18	2.46	54	1125.2833	0.3700	6
1.46	18	2.46	78	1125.2857	0.3697	6
1.46	18	2.46	114	1118.3570	0.3709	6
1.46	26	1.69	54	1100.9804	0.3736	6
1.46	26	1.69	78	1104.0403	0.3730	6
1.46	26	1.69	114	1106.6723	0.3725	6
1.46	26	2	54	1102.7815	0.3734	6
1.46	26	2	78	1106.3295	0.3730	6
1.46	26	2	114	1102.5365	0.3732	6
1.46	26	2.46	54	1104.8694	0.3730	6
1.46	26	2.46	78	1100.3125	0.3736	6
1.46	26	2.46	114	1101.9713	0.3734	6
1.46	38	1.69	54	1095.1796	0.3747	7
1.46	38	1.69	78	1093.4396	0.3749	7
1.46	38	1.69	114	1097.1749	0.3743	7
1.46	38	2	54	1097.0867	0.3743	7
1.46	38	2	78	1097.1580	0.3743	7
1.46	38	2	114	1095.5828	0.3747	7
1.46	38	2.46	54	1095.3275	0.3747	8
1.46	38	2.46	78	1099.0972	0.3743	7
1.46	38	2.46	114	1094.7728	0.3748	7